Wind-Driven Flow over Topography in a Zonal β-Plane Channel: A Quasi-geostrophic Model of the Antarctic Circumpolar Current

J.-O. WOLFF AND E. MAIER-REIMER

Max-Planck-Institut für Meteorologie, Hamburg, Germany

D. J. OLBERS

Alfred-Wegener-Institut für Polar- und Meeresforschung, Bremerhaven, Germany

ABSTRACT

The paper gives a detailed account of the dynamical balance of a wind-driven zonally unbounded flow over topography. The problem is investigated with a quasi-geostrophic β-plane channel with two layers and eddy resolution. The channel has a width of 1500 km and a zonal periodicity of 4000 km. Apart from the dimensions, the model structure is similar to the one used by McWilliams et al. The experiments with this model address the problem of the relative role of transient and standing eddies as well as bottom friction and topographic form stress in the balance of a current driven by a steady surface windstress. The response of the system is investigated for different values of the friction parameter and various locations of topographic obstacles in the bottom layer of the channel. The principal momentum balance emerging from these experiments supports the concept of Munk and Palmén for the dynamics of the Antarctic Circumpolar Current, which proposes that the momentum input by windstress is transferred to the deep ocean—in the present model by vigorous eddy activity—where it leaves the system by topographic form stress. Frictional effects in the balance of the circumpolar flow may thus be of minor importance. This concept of the momentum balance is confirmed in simulations over more complex topographies. Here we have taken two differently scaled versions of the highly resolved bottom relief in the Macquarie Ridge area. The flow in these simulations is virtually frictionless in the momentum balance. The flow pattern reflects some features of the Circumpolar Current in this area.

1. Introduction

Our theoretical understanding of the ocean circulation and the dynamical balance of current systems is largely oriented at the large-scale, wind-driven flow in ocean basins. This large-scale flow is not strongly affected by topography or detailed structures of small-scale dissipation mechanisms, and is generally governed by Sverdrup-type dynamics with some sort of boundary layers. Of course, each current has its peculiarities but the one that is atypical in most aspects is the Antarctic Circumpolar Current (ACC). The ACC is the longest (about 24 000 km) and most intensive current [transport about 130 Sv (1 Sv ≡ 10^6 m³ s⁻¹)] of the World Ocean. It flows almost unconstrained by any significant continental barriers in the only zonally unbounded region of the World Ocean. Here Sverdrupian dynamics do not apply. The current is evidently wind-driven; nevertheless it extends with a strong barotropic component down to the bottom, and the path of the current

clearly shows the influences of the midocean ridges, plateaus, and sea mounts in the Southern Ocean (e.g., see the dynamic topographies of Gordon et al. 1978, or the β-spiral model of Olbers and Wenzel 1989).

A further important feature of the Southern Ocean—and another difference to most other oceanic regions—is the presence of a vigorous eddy field (e.g., see Patterson 1985; Cheney et al. 1983; Koblinsky 1988) which is related to the dynamics of the ACC and the heat and tracer transports. Contrary to the conditions in the ocean basins to the north, there is convincing observational evidence for a large contribution of the eddy field to the meridional heat transport in the Southern Ocean (de Szoeke and Levine 1981; see also the review by Bryden 1983). The suggestion that eddies may also play a significant role in the dynamics of the ACC is, however, mainly based on theoretical grounds. The basic numerical investigations in this direction have been performed by J. McWilliams and W. Holland with quasi-geostrophic (QG) models of the flow in a zonal channel on a β-plane (McWilliams et al. 1978; McWilliams and Chow 1981). The work on the role of topography and mesoscale eddies in the dynamical balance of the ACC that we present here is an extension of the results of McWilliams et al. (1978).

Corresponding author address: Dr. Jörg Olaf Wolff, Max-Planck-Institut für Meterologie, Bundesstr. 55, 2000 Hamburg 13, Germany.

Some preliminary results were presented in Wolff and Olbers (1989).

The dynamical balance of the ACC has long been considered a mystery. Unlike other current systems the problem with the ACC is not to identify the basic driving mechanism but rather to find the sink for the momentum that is imparted to the ocean by the surface windstress. In the latitude band of the Drake Passage, there are no continental barriers that could support a net zonal pressure gradient and thereby oppose the acceleration of the current by the wind. Large-scale models of flow in a zonal channel with the usual diffusive parameterization of momentum transport by eddies or reasonable magnitudes of bottom friction gave rather unsatisfactory results (Hidaka and Tsuchiya 1953; Gill 1968; and others). The current amplitudes in these models are proportional to the applied windstress and inversely proportional to the values of the frictional parameters; e.g., for lateral friction the transport scales as $\tau \cdot D^3/A$ where τ is the windstress amplitude, D the current width, and A the lateral viscosity. Hidaka faced the difficulty of explaining the observed transport values with reasonable values for the model friction and given the constraint of the observed windstress. The traditionally accepted values for horizontal and vertical eddy viscosity result in transport values for the ACC which are an order of magnitude or more above the observed values in the Drake Passage, and conversely, the fit of the models to the observed transport requires unrealistically large eddy coefficients (for $\tau = 10^{-4}$ m^2 s^{-2} and $D = 1000$ km a transport of 10^8 m^3 s^{-1} yields an A of 10^6 m^2 s^{-1}). This implies a meridional momentum transport of the order 0.1 m^2 s^{-2}, which is far larger than any reasonable value estimated from data anywhere in the ocean. On the northern flank of the ACC Bryden and Heath (1985) observed values of 10^{-2} to 10^{-3} m^2 s^{-2}. This is in the eddy active area of the Macquarie Ridge Complex and thus on the larger side of the range of possible values.

One of the earliest papers on this problem (Munk and Palmén 1951) suggested a solution which today still appears as the only acceptable way out of a highly frictionally controlled balance of the current. Though continental barriers are absent, there are significant submarine ridges to build up net zonal pressure gradients. This could enable transfer of horizontal momentum to the solid earth. A balance with the windstress can occur only if the flow establishes pressure differences across the ridges with the appropriate sign (higher pressure value on the western side for westerly winds) and magnitude. To balance a stress of 10^{-4} m^2 s^{-2} (a typical observed value in the belt of polar westerlies) a pressure difference of only a few dynamic centimeters is required across a ridge of a few thousand kilometers. Furthermore, the momentum given to the ocean at the surface must be transferred down to the blocked depths where flux by pressure differences across topography—the so called topographic form stress or

mountain drag—can be effective. This transport of momentum must be extremely large compared to other oceanic areas. To transmit the windstress of the above magnitude in the observed vertical current shear (0.1 m s^{-1} over 1000 m) by vertical diffusion, a value of vertical eddy viscosity of 1 m^2 s^{-1} is needed. This is two or even three orders of magnitude larger than elsewhere (large-scale oceanic models generally use 10^{-4} m^2 s^{-1}).

Both requirements in this momentum balance cannot at present be tested against observations. The determination of the topographic form stress requires measurements of bottom pressure differences with an accuracy of one dynamic centimeter, which is far beyond present capabilities. The accurate measurement of the vertical eddy flux of horizontal momentum—i.e., the correlation between the vertical and horizontal velocity fluctuations—is a traditional problem that is still on the margin of the present observational technology. Models thus appear to offer the only way to a solution.

Unfortunately, model answers depend strongly on the resolution. Ocean circulation models with coarse resolution (grid size much larger than the eddy scale) did not substantiate the balance proposed by Munk and Palmén, whereas eddy resolving models support this concept.

One of the early coarse model studies is the set of experiments reported by Gill and Bryan (1971). Here the combined action of topography (or the idealized submarine ridge in form of the submerged sluice gate in the Drake Passage) and baroclinicity increased the flow; i.e., the topographic form stress worked with the wind to accelerate the current even more in the eastward direction. The reason was found in a thermal difference across the ridge in the Drake Passage, which was generated by water mass formation processes. The relevance of this result was questioned since numerical constraints allowed the ocean in this experiment to rotate at only a tenth of the true rotation rate.

The series of experiments of Bryan and Cox (1972) and Cox (1975) with a coarse global ocean circulation model ($2° \times 2°$ horizontal resolution with eddy viscosities of 10^{-4} m^2 s^{-1} and 4×10^4 m^2 s^{-1} for vertical and horizontal momentum transport) are harder to interpret. The first experiment with a flat bottom homogeneous ocean clearly demonstrates Hidaka's dilemma: the transport through the Drake Passage was 600 Sv after 90 days of integration and was still increasing (the experiment was not run to a steady state). The introduction of the topography reduces the transport drastically to only 22 Sv. Hidaka's dilemma is circumvented here by the peculiar pattern of the contours of planetary vorticity f/H in the region of the Drake Passage; the sill in this passage expells almost all contours. The few which pass must stick to the continental margins and thus run far into the adjacent ocean basins to the north. Since the barotropic flow

must follow f/H contours (in case of weak forcing and dissipation) the circumpolar current in the homogeneous topographic ocean resides predominantly in the basins north of the circumpolar belt, where the wind can be balanced by net zonal pressure forces and Sverdrup dynamics apply. In the experiments which include the baroclinicity the ACC has a transport of 180 Sv. Though the solution presented in Cox's (1975) paper is definitely not in equilibrium, we can draw the conclusion that the baroclinicity enables the system to increase the transport of the ACC. This is confirmed by other investigations with numerical global models following Bryan and Cox's work.

The main reason why coarse resolution models do not support the balance concept of Munk and Palmén (1951) can be found in the parameterization of the turbulent momentum transport. All of these models use diffusive parameterizations with vertical viscosities in the traditional range 10^{-4} to 10^{-3} m^2 s^{-1} and very large horizontal viscosities dictated by consideration of boundary layer resolution [a 5° resolution such as that of Han (1984) requires 8×10^5 m^2 s^{-1}, which is quite in the uncomfortable range of Hidaka's dilemma]. Although the models approximately reproduce the observed vertical current shear, the momentum flux in the ocean is not comparable to the wind-stress because of the low vertical viscosity. The wind input must diffuse away laterally and leave the Southern Ocean to the northern basins or at the continental boundaries of Antarctica. The topographic form stress is thus not required to act as an effective sink of momentum. The baroclinic field may thus evolve quite independently from the constraint of the overall momentum balance of the current.

The work of McWilliams et al. (1978) describes a set of eddy resolving experiments for a wind-driven channel flow over topography. They use a two-layer quasi-geostrophic model of a wind-driven flow in a zonal channel. In some experiments, partial meridional barriers represent a Drake Passage. Lateral boundary conditions allow the flow to move freely along the walls, while the bottom is frictional. There are two experiments related to the role of the topographic form stress: one has a flat bottom and one has idealized topography in the center of the passage—a small Gaussian-shaped mount entirely contained in the deep layer. The flat bottom case reflects Hidaka's dilemma: the friction at the model bottom is too low to constrain the transport through the gap from reaching values exceeding 600 Sv. The balance of the zonal momentum resulting for the topographic case is in good agreement with Munk and Palmén's concept: in the passage the upper layer momentum is in balance between the wind input and the interfacial form stress, which transfers the momentum to the deep layer where it leaves the system via the topographic form stress. The transport stays below 100 Sv. The interfacial form stress is entirely due to standing and transient eddies, the latter being vigor-

ously fed by the baroclinic instability of the mean current. It is worth noting that the lateral Reynolds stresses exerted by the eddies on the mean flow tend to transfer eastward momentum into the center of the eastward current and concentrate the jet, quite in contrast to the outward momentum diffusion that is inherent in coarse models.

The present paper reports on similar eddy resolving experiments in channel geometry. We compare experiments with different values of the bottom frictional parameter and various simple topographies with a basic case that is similar to the above-described topographic experiment of McWilliams et al. (1978). Particular emphasis is placed on a detailed analysis of the spinup and the balance of the time and zonally averaged zonal momentum in all experiments. We supplement this investigation with two experiments that use the highly resolved bathymetry of the Macquarie Ridge Complex southwest of New Zealand as the topography in the otherwise unchanged QG-channel. The topography consists of the spiked ridge (extending over only a few gridpoints), the broad Campbell Plateau, and random hills on a bottom that gently undulates on the large scale. These experiments appear to us as the first attempts to use realistic topography in a QG-model and compare the results with observations. The momentum and vorticity balance in these two experiments can be related to the investigations on quasi-geostrophic flow over artificial random topography by Treguier and McWilliams (1990).

2. The quasi-geostrophic channel model

We consider a rotating, hydrostatic, adiabatic fluid with two immiscible layers $i = 1, 2$ of different densities ρ_i and mean layer thicknesses H_i in a zonal channel of length X and width Y. The actual layer thicknesses are

$$d_1 = H_1 - \eta + \zeta \tag{1}$$

$$d_2 = H_2 + \eta - B \tag{2}$$

where ζ is the displacement of the surface and η the displacement of the interface from their mean positions; $B(x, y)$ is the bottom topography (positive if above the mean depth $H_1 + H_2$).

a. The model equations

We assume quasi-geostrophic dynamics on a β-plane. In most aspects the numerical model is identical to the one described by McWilliams et al. (1978). The flow is governed by the balance of potential vorticity in each layer

$$\frac{\partial q_i}{\partial t} + J(\psi_i, q_i) = F_i \tag{3}$$

where the indices $i = 1, 2$ denote the upper and the lower layer, respectively. The potential vorticities are given by

$$q_1 = H_1\nabla^2\psi_1 - \frac{f_0^2}{g'}(\psi_1 - \psi_2) + H_1 f \qquad (4)$$

$$q_2 = H_2\nabla^2\psi_2 + \frac{f_0^2}{g'}(\psi_1 - \psi_2) + H_2 f + f_0 B \qquad (5)$$

and the ψ_i are streamfunctions of the geostrophic velocity in each layer. Furthermore, $f = f_0 + \beta(y - y_0)$ is the Coriolis frequency in the channel with the mid-latitude y_0 and $g' = g(\rho_2 - \rho_1)/\rho_1$ as the reduced gravity.

The flow is forced by a windstress τ. The energy can be dissipated mainly by bottom friction (with a decay time ϵ^{-1}) and to a lesser extent by lateral friction that is parameterized here in a biharmonic form to act predominantly on small grid scales. The forcing terms in (3) are thus given by

$$F_1 = \text{curl}\tau - A_4 H_1\nabla^6\psi_1 \qquad (6)$$

$$F_2 = -\epsilon H_2\nabla^2\psi_2 - A_4 H_2\nabla^6\psi_2. \qquad (7)$$

All quantities are assumed to be periodic with the basin length X. The boundary conditions on the southern and northern channel walls at $y = y_S$ (the Antarctic coastline) and $y = y_N$ are

$$\psi_i = \text{const} \quad \text{and} \quad \nabla^2\psi_i = \nabla^4\psi_i = 0. \qquad (8)$$

These conditions assure that there is no geostrophic flow through the solid walls and no sources or sinks of momentum or volume-integrated energy at these boundaries.

The values of the streamfunctions on the walls determine the total flow through the channel. These four values are not yet fixed by (8). The vorticity dynamics have lost this information (formally by elimination of the ageostrophic pressure field and neglection of the kinematic boundary conditions for the ageostrophic velocities). As shown by McWilliams (1977) a complete set of supplementary conditions may be derived from the consideration of the first-order (ageostrophic) zonal momentum balance and the mass balance of both layers by requiring that the ageostrophic pressure field is uniquely defined. We have adopted the formulation of the supplementary constraints given in McWilliams et al. (1978).

b. Numerics and model specification

The numerical integration of the model equations uses standard, second-order finite-difference discretizations on an Arakawa-C-type grid for velocities and streamfunction. For the calculation of the Jacobian, an energy and enstrophy conserving formulation is used (Arakawa and Lamb 1977). The time discretization was done with the leap-frog method where three timesteps are mutually connected. To avoid time splitting of the developing solutions a projection of the timesteps $n + 1$ and $n - 1$ on the timestep n was performed every 100 timesteps. The bottom friction and viscosity terms are calculated at the time level $n - 1$

to avoid (linear) numerical instability (Richtmyer 1967).

The experiments considered here (see Tables 1 and 2) are carried out in a periodic circumpolar two-layered channel with 1500 km width and 4000 km length centered at 60°S. The southern boundary of the channel is viewed as an idealized coastline of Antarctica. The mean depths of the two layers are 1000 m for the upper layer and 4000 m for the lower layer. The topography is always entirely contained in the lower layer with maximum heights of 500 m and in most cases it has the form of simple Gaussian mounts or ridges with a zonal e-folding scale of 150 km. Exceptions are the experiments M1 and M2 which use a scaled form of the Macquarie Ridge area with the Campbell Plateau with maximum heights 500 and 1500 m, respectively.

The biharmonic friction parameter is $A_4 = 10^{10}$ m^4 s^{-1}. For the values of the bottom friction parameter in the following experiments ($\epsilon = 10^{-7}$ s^{-1} and $\epsilon = 6 \times 10^{-7}$ s^{-1}) bottom friction is the dominating effect. The spindown times are $\epsilon^{-1} \approx 116$ days and 19 days, respectively, whereas the lateral friction has a spindown time of $A_4^{-1}Y^4 \approx 3 \times 10^6$ years (channel scale flow) or $A_4^{-1}(\Delta x)^4 \approx 170$ days (gridsize $\Delta x = 20$ km). The timestep was chosen to be 2 hours.

The zonal windstress τ is assumed to be zonally constant and meridionally varying in a sinusoidal shape:

$$\tau = \tau_0 \sin\left(\frac{\pi y}{Y}\right), \qquad (9)$$

with a maximum amplitude $\tau_0 = 10^{-4}$ m^2 s^{-2} at the central latitude of the model area. The reduced gravity $g' = g\Delta\rho/\rho$ is 0.02 m s^{-2}, which results in a baroclinic Rossby radius $R_1 = [g'H_1H_2/(H_1 + H_2)]^{1/2}f_0^{-1}$ of 32 km. This is far too large for the Southern Ocean where R_1 may become as small as 10 km (Houry et al. 1987) but in view of the great variety of experiments a higher resolution would have been beyond our computational limits.

3. The momentum balance in a zonal channel: flat bottom vs. topography

The flow in the channel is entirely driven by the windstress and—if the model achieves a steady or quasi-steady state—the total momentum imparted at the surface $(2\tau_0 XY/\pi)$ has to leave the system, at least in the time average. Since there is no lateral friction at the boundaries this has to occur entirely through the bottom. The flux of momentum through the interface must thus equal the flux through the surface, no matter how the dynamics achieve this. Consider the balance of the momentum $d_i(u_i, v_i)$ and mass d_i ($i = 1, 2$) given by

$$\frac{\partial}{\partial t}(d_i\mathbf{v}_i) + \nabla(\mathbf{v}_i d_i\mathbf{v}_i) + f\mathbf{k} \times d_i\mathbf{v}_i$$

$$= -d_i\nabla p_i + (\vec{\tau}_U - \vec{\tau}_L)_i - A_4\nabla^4(d_i\mathbf{v}_i) \qquad (10)$$

$$\frac{\partial}{\partial t} d_i + \operatorname{div}(\mathbf{v}_i d_i) = 0 \qquad (11)$$

where d_i are the layer thicknesses. The pressure fields (per unit density) are $p_1 = g\zeta$ and $p_2 = g\zeta + g'\eta$ where ζ and η are the surface and interface deviations, respectively. For the upper layer $\vec{\tau}_U$ is the windstress $\vec{\tau}$, and $\vec{\tau}_L$ is an interfacial frictional stress $\vec{\tau}_I$, whereas for the lower layer $\vec{\tau}_U = \vec{\tau}_I$ and $\vec{\tau}_L = \epsilon d_2 \mathbf{v}_2$, the bottom frictional stress.

a. Interfacial form stress

In the absence of interfacial friction ($\vec{\tau}_I \equiv 0$) as considered in our model, the only mechanism for exchange of momentum is the flux associated with the horizontal pressure force acting across the inclined interface (the interfacial form stress). Integrating the momentum balance (10) over the entire area of the channel reveals the importance of this term. If a quasi-steady state is reached, the mass balance implies the vanishing of the net meridional mass flux in the channel at each latitude

$$\left\langle \overline{d_i v_i} \right\rangle = \frac{1}{XT} \int_0^X \int_0^T d_i v_i \, dt \, dx = 0. \qquad (12)$$

We have denoted the time average by an overbar and the zonal average by angle brackets. The zonal component of the momentum balance in the two layers then becomes

$$\int_0^Y \left\langle \overline{g\eta \frac{\partial \zeta}{\partial x} + \tau} \right\rangle dy = 0 \qquad (13)$$

$$\int_0^Y \left\langle \overline{B \frac{\partial}{\partial x}(g\zeta + g'\eta) - g\eta \frac{\partial}{\partial x}\zeta - \epsilon d_2 u_2} \right\rangle dy = 0 \qquad (14)$$

while the meridional component reflects a geostrophic balance with bottom friction in the lower layer. Equations (13) and (14) indicate that a steady state can only exist in the presence of zonal deformations of the surface and the interface. A nonzero interfacial form stress

$$\int_0^Y \left\langle \overline{\eta \frac{\partial}{\partial x}\zeta} \right\rangle dy = -\int_0^Y \left\langle \overline{\zeta \frac{\partial}{\partial x}\eta} \right\rangle dy \qquad (15)$$

can only result if there are zonal deformations of η and ζ that are out of phase.

This is clearly demonstrated by experiment FB (see Table 2) with the QG model described above. Case FB has a flat bottom and is driven by an eastward windstress of the form (9). Starting from rest, a smooth zonal flow develops in both layers that resembles the meridional structure of the windstress. There are no zonal gradients of pressure (or any other quantity) and the lower layer obtains its zonal momentum entirely from the mass changes in the channel (deepening of the upper layer in the southern half and flattening in
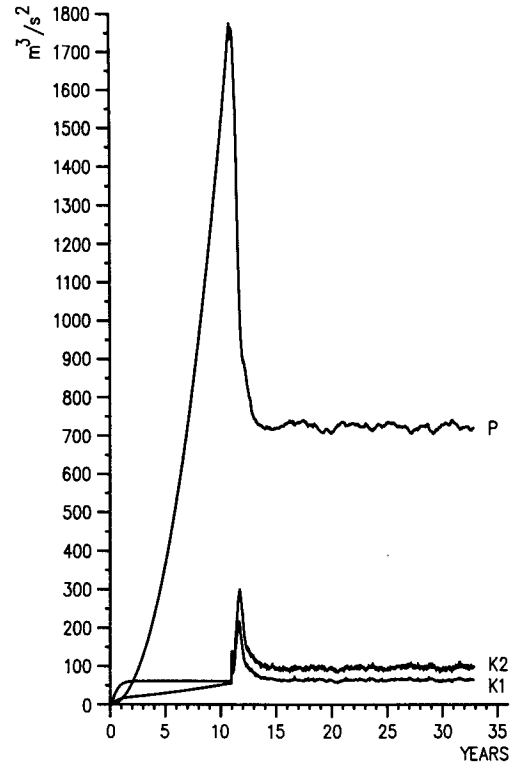

FIG. 1. Case FB: Time series of the area averaged potential (P) and layer kinetic energies (K1, K2). Units are $m^3 \, s^{-2}$. The change in the time development after 11 years is initiated by an externally imposed disturbance.

the northern half of the channel) associated with the meridional cell that is driven by the Ekman flow. Figure 1 displays the time history of the potential and the kinetic energies. The above-described zonally uniform phase of the experiment extends over the first 11 years. Both the meridional slope of the interface and the zonal velocity in the upper layer increase linearly with time, as is manifested by an increase of the potential energy $P = g'\eta^2/2$ and the kinetic energy $K_1 = d_1(u_1^2 + v_1^2)/2$. The kinetic energy in the lower layer, $K_2 = d_2(u_2^2 + v_2^2)/2$, remains constant after the initial spinup. An analytical solution of this spinup phase can be derived from the linearized form of the equations (10). Neglecting the lateral friction terms we find for initial conditions $u_i = v_i = \eta = \zeta = 0$ at $t = 0$, and the windstress given by (9)

$$u_1 = (1 - e^{-\lambda t})U \sin(ky) + t\frac{g'k^2\tau_0}{f^2}\sin(ky)$$

$$u_2 = (1 - e^{-\lambda t})U \sin(ky)$$

$$v_1 = \left(\frac{-1}{fH_1} + \frac{g'k^2}{f^3}\right)\tau_0 \sin(ky) + \frac{\lambda}{f}e^{-\lambda t}U \sin(ky)$$

$$v_2 = \left(\frac{\tau_0}{fH_2}\right)(1 - e^{-\lambda t}) + \left(\frac{\lambda}{f}e^{-\lambda t}\right)U \sin(ky)$$

$$\eta = -t \cdot \frac{\tau_0}{f} k \cos(ky)$$

$$\zeta = \left(\frac{f}{gk}\right)[1 - e^{-\lambda t}] U \cos(ky) - t \frac{g'\tau_0}{gf} k \cos(ky)$$

$$(16)$$

with $k = \pi/Y$ and

$$\lambda = \frac{\epsilon k^2 H_2}{k^2(H_1 + H_2) + f^2/g} \approx \frac{\epsilon H_2}{H_1 + H_2}. \quad (17)$$

For small times, $\lambda t < 1$ (or $t < 144$ days for our set-up), the solution describes the spinup of a barotropic state with the amplitude

$$U = \frac{\tau_0}{\epsilon H_2} \quad (18)$$

of the zonal current u_i and a northward Ekman transport in the upper layer that is compensated by frictional flow in the deep layer. Then, for $\lambda t \gg 1$, the zonal current in the upper layer and the interface start to grow linearly and the system becomes baroclinic. Notice that the interfacial form stress of this state is zero. This analytical solution does not contain developing boundary layer solutions due to the biharmonic lateral friction parameterization (see the Appendix for a discussion of the structure of these boundary solutions).

Unless the flow becomes unstable and generates its own nonzonal perturbations, this growth phase would continue until the upper layer eventually runs out of mass at the southern boundary (or the lower layer at the northern boundary depending on the choice of the mean layer depths) and the windstress is directly transmitted into the lower layer where it can be compensated by bottom friction. Then the system may eventually come to a steady state.

The QG model, however, is incapable of simulating this transition since the actual thicknesses are not directly seen by quasi-geostrophic dynamics (they may in fact become negative without any numerical problems). After 11 years the interface has dropped about 750 m at the northern boundary (actual layer depth 1750 m) and the maximum of the zonal velocities is 0.44 m s^{-1} in the upper layer and 0.25 m s^{-1} in the lower layer. The upper layer transport is 475 Sv and the deep layer transport (949 Sv) has almost acquired the steady state value of 955 Sv in agreement with (16). The flow is baroclinically unstable and a slight perturbation introduced in the center of the channel immediately leads to the development of a vigorous eddy field and strong meanders in the current (see Fig. 2). A transition to a quasi-steady state with much lower potential energy takes place within about 3 years (the advective time scale through the channel is about 1 year). In the time-mean the zonal jet is strongly concentrated in the latitudes of the windstress maximum and differs significantly from the sinusoidal profiles of

the laminar flow during the spinup phase. Even in this fully turbulent regime the lower layer transport is constrained by the balance of the total momentum obtained from (13) and (14) for $B = 0$ (Treguier and McWilliams 1990):

$$\int_0^Y \langle \overline{d_2 u_2} \rangle dy = \frac{2\tau_0 Y}{\epsilon \pi} = 955 \text{ Sv.} \quad (19)$$

This relation reflects Hidaka's dilemma discussed in the Introduction; the transport is inversely proportional to the bottom friction parameter. The simulation yields an average transport of 982 Sv over the last 11 years, which deviates by about 2%–3% from (19). By extending the averaging interval this discrepancy can be further reduced. Detailed analysis showed that there is an uncertainty of 1%–2% in the value of the average transport if computed over an interval of 10 to 20 years.

Apparently, in this second phase of the experiment the form stress at the interface is activated by the nonzonal perturbations of the surface and the interface, and the overall balances (13) and (14) of zonal momentum are now appropriate. Since in the zonally homogeneous system FB the time-mean flow must be zonal, the interfacial form stress is entirely carried by the transient eddy part of the flow defined as the deviation from the time-mean:

$$\psi_i' = \psi_i - \overline{\psi_i}. \quad (20)$$

If the zonally homogeneous configuration of the channel is perturbed by introduction of topography $B(x, y)$ in the lower layer, the time-mean flow may also contribute to the interfacial form stress because the standing eddy part

$$\psi_{*i} = \overline{\psi_i} - \langle \overline{\psi_i} \rangle \quad (21)$$

will be nonzero. This is illustrated in Fig. 3, which shows the mean flow (time average over the last 11 years) and standing eddy part for both layers of case SC. There is a mount in the center of the channel (slightly displaced to the south, see Table 2) that splits the mean flow in both layers into a strong northern jet and a weaker jet in the southern part of the channel. The topography tends to concentrate the northern jet and deflects it to the south. Downstream of the topography barrier it broadens again with a superimposed standing lee wave pattern. This time-mean solution shows remarkable similarities to the analytical solution for the flow of a zonal current over an isolated seamount of McCartney (1976) and Spillane (1978). The time-mean transports of case SC are 168 Sv for the upper layer and 198 Sv for the lower layer with maximum zonal velocities of 0.26 and 0.12 m s^{-1}, respectively. The instantaneous flow field is characterized by a vigorous eddy field in both layers and a greatly deformed surface and layer interface.
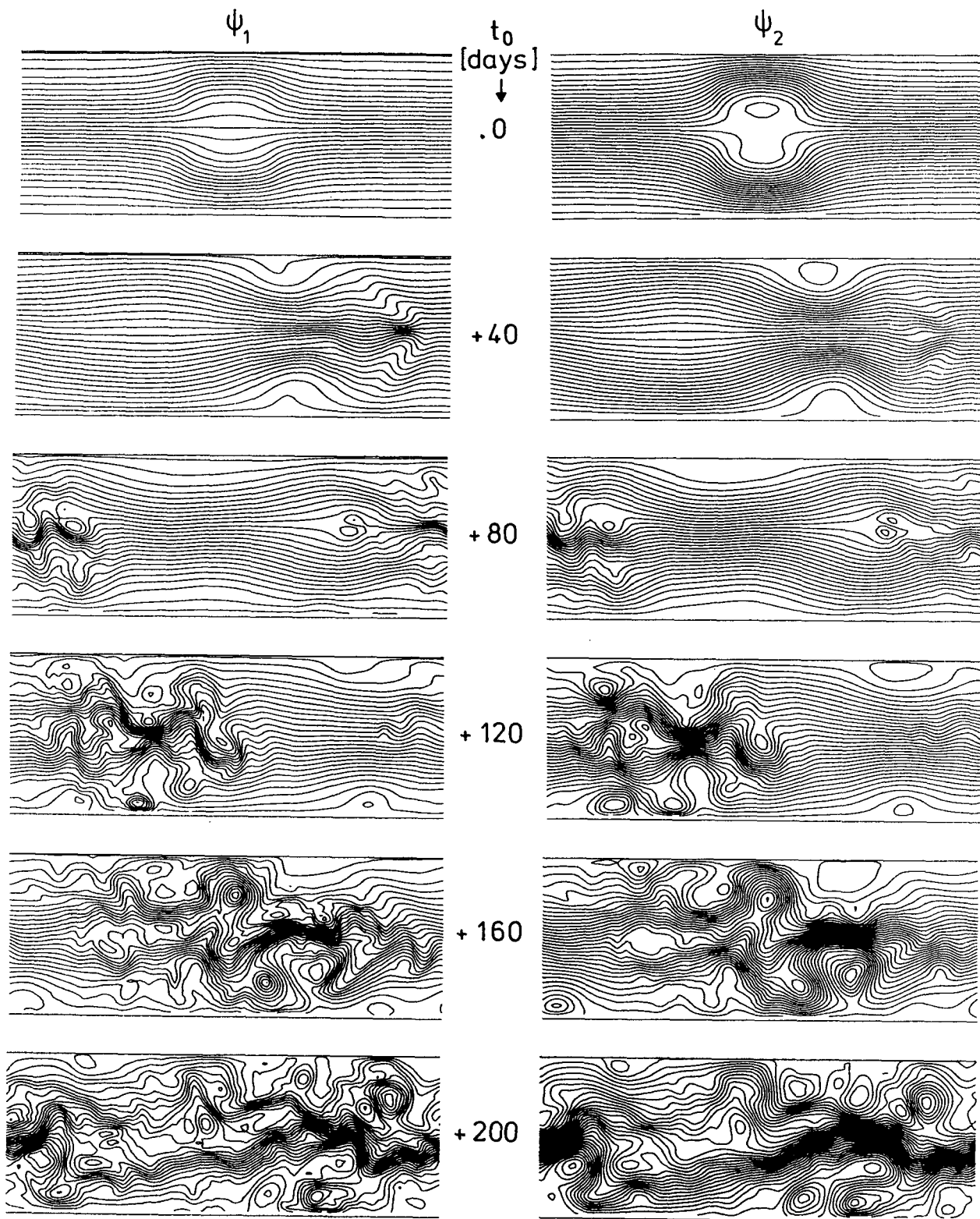
FIG. 2. Case FB: Time series of upper layer streamfunction (left column) and lower layer streamfunction (right column) after the perturbation. Shown are 40 day intervals from top to bottom. Contour intervals are 2×10^4 and 10^4 m^2 s^{-1} for the upper and lower layer, respectively.
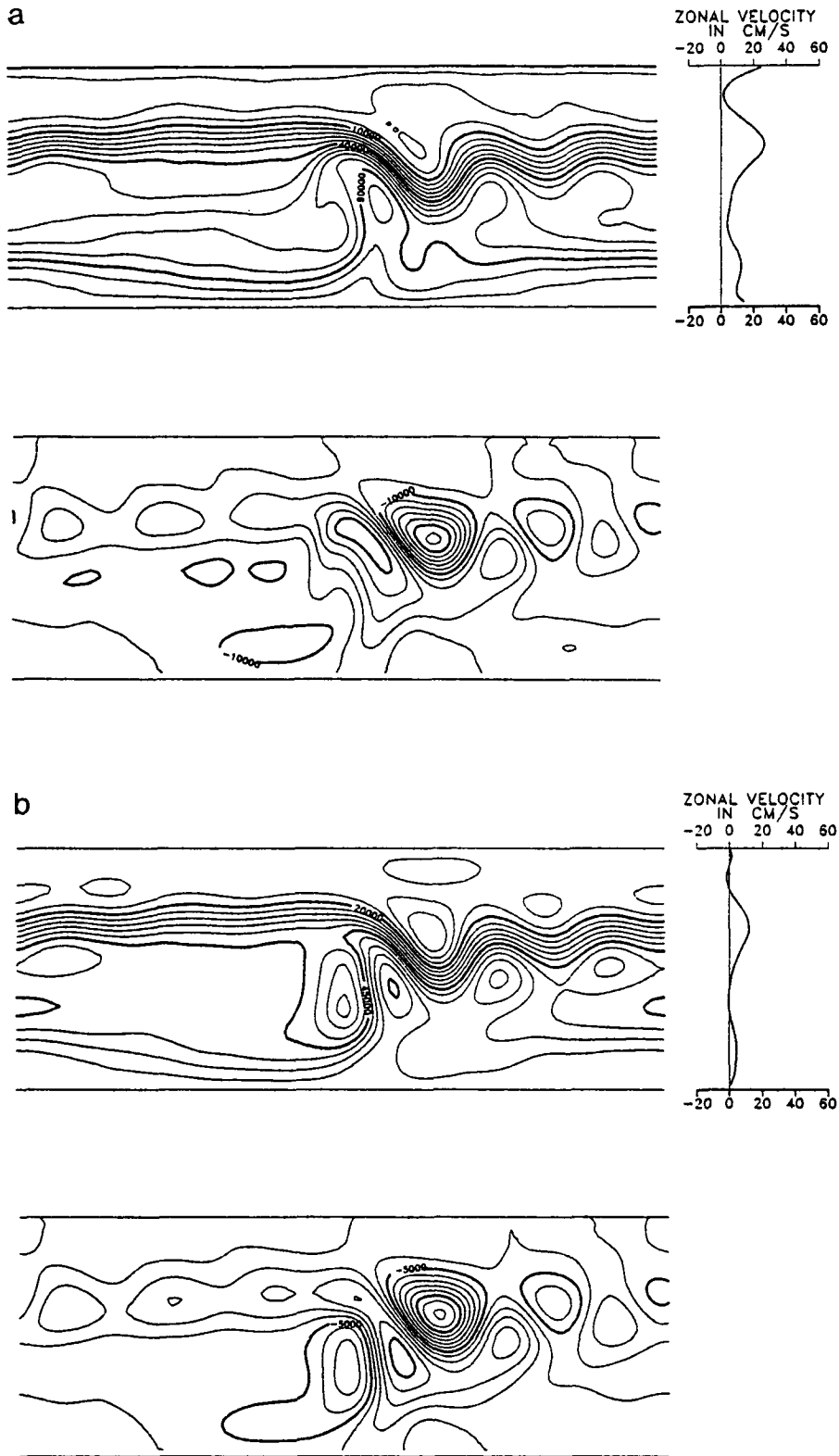
a

b

FIG. 3. Case SC: Time-mean streamfunctions (averaged from 22 to 33 years) with the time and zonal-mean zonal velocity distribution (top) and time-mean standing eddies (bottom). (a) Upper layer and (b) lower layer fields. Upper layers: $CI = 10^4 \, m^2 \, s^{-1}$. Lower layers: $CI = 5 \times 10^3 \, m^2 \, s^{-1}$. Velocities are in cm s^{-1}.

b. Topographic form stress

The standing eddies not only contribute to the momentum transfer through the interface but also create the only other mechanism, besides bottom friction, for an exchange of momentum with the bottom. The topographic form stress:

$$\int_0^Y \left\langle B \frac{\partial}{\partial x} \left(g\bar{\zeta} + g'\bar{\eta} \right) \right\rangle dy = \int_0^Y \left\langle B \frac{\partial \bar{p_2}}{\partial x} \right\rangle dy \quad (22)$$

is entirely caused by the nonzonal time-mean flow, i.e., the standing eddies. It is nonzero if there are zonal pressure differences across the topographic obstacles. A higher pressure on the western side of ridges corresponds to a flux of eastward momentum into the bottom. Equating $(\partial p_2/\partial x)f^{-1}$ with the meridional geostrophic flow $v_2^{(0)}$ this condition requires northward $v_2^{(0)}$ over a ridge in the Southern Hemisphere. The standing eddy pattern in the deep layer of case SC (Fig. 3) indeed reflects this situation.

The simple formula (19) no longer holds in the presence of topographic obstacles. The balance of the total momentum in the channel

$$\int_0^Y \left\langle \overline{d_2 u_2} \right\rangle dy = \frac{2\tau_0 Y}{\epsilon \pi} + \frac{1}{\epsilon} \int_0^Y \left\langle B \frac{\partial \bar{p_2}}{\partial x} \right\rangle dy \quad (23)$$

now includes the topographic form stress, and the transport in the deeper layer is no longer entirely given by the external parameters τ_0 and ϵ. The flow is generally expected to organize the deep-layer pressure field such that the topographic form stress $\langle B\partial\bar{p_2}/\partial x \rangle$ opposes the applied forcing at the surface (the hypothesis of Munk and Palmén 1951), and furthermore, that it acts as a drag—i.e., opposes the deep mean flow. The first statement is true for all our experiments; the second, however, has important exceptions as discussed below (section 5d).

c. The time and zonal average momentum balance

In the following we will describe and analyze experiments with the quasi-geostrophic model for various cases of different topography and two numerical values of the bottom friction parameter. Table 1 summarizes the external parameters and some bulk quantities characterizing the resulting flows are listed in Table 3. As a basic analysis tool we use the balance of the zonal momentum in each layer, closely following Mc-Williams et al. (1978). The balance (10) is averaged in time (over the last 11 years of each experiment) and along the entire channel, thus restricting our interest to the time and zonal average momentum in the quasistationary state. Since $\langle \overline{d_i v_i} \rangle = 0$ (see 12) we notice that only the advective, pressure and friction terms remain in the balance. With no explicit vertical momentum diffusion (i.e., $\tau_I \equiv 0$) as considered here in the eddy resolving experiments, the only net transport of mean momentum from the surface layer to the deeper layer is by the interfacial form stress. The balance of the mean zonal momentum in the upper layer is then expressed as

$$\left\langle \frac{\partial}{\partial y} \overline{v_1 d_1 u_1} \right\rangle = g\left\langle \overline{\eta \frac{\partial \bar{\zeta}}{\partial x}} \right\rangle + \langle \bar{\tau} \rangle - A_4 \langle \overline{\nabla^4 d_1 u_1} \rangle \quad (24)$$

while in the lower layer the pressure term splits into the interfacial and the bottom form stresses:

$$\left\langle \frac{\partial}{\partial y} \overline{v_2 d_2 u_2} \right\rangle = -g\left\langle \overline{\eta \frac{\partial \bar{\zeta}}{\partial x}} \right\rangle + \left\langle B \frac{\partial}{\partial x} \left(g\bar{\zeta} + g'\bar{\eta} \right) \right\rangle$$
$$- \epsilon \langle \overline{d_2 u_2} \rangle - A_4 \langle \overline{\nabla^4 d_2 u_2} \rangle. \quad (25)$$

The actual layer thicknesses d_i may be replaced here by the constant mean values H_i. It should be noted that these balances of the mean zonally averaged momentum are effectively statements about the vorticity dynamics of the system. It can be shown, using the auxiliary conditions of McWilliams (1977) in the original momentum form, that Eqs. (24) and (25) are the balance of the time-averaged circulation around a loop consisting of the respective latitude line, the northern or southern boundary, and closing meridional sections at the periodic eastern and western boundaries. Equivalently, these equations represent the balance of the

TABLE 1. Model parameters.

Model parameter			
Upper layer depth	$H_1 = 1000$ m	Channel length	$X = 4000$ km
Lower layer depth	$H_2 = 4000$ m	Channel width	$Y = 1500$ km
Gridsize	$\Delta x = \Delta y = 20$ km	Timestep	$\Delta t = 2$ hours
Central latitude	60°S	Coriolis parameter of reference latitude	$f_0 = -1.263 \cdot 10^{-4}$ s^{-1}
Reduced gravity	$g' = 0.02$ m s^{-2}		
Bottom friction parameter (except HF)	$\epsilon = 10^{-7}$ s^{-1}	1. baroclinic Rossby-radius	$R_1 = 32$ km
		Biharmonic friction parameter	$A_4 = 10^{10}$ m^4 s^{-1}
Maximum windstress	$\tau = 10^{-4}$ m^2 s^{-2}	Topographic anomaly amplitude (except M2)	$B_0 = 500$ m

time-averaged vorticity, integrated over the area enclosed by this loop.

Using the quasi-geostrophic approximations in (24) and (25) and partitioning the flow into the time-averaged parts $\bar{\psi}_i$ and the transient and standing eddy parts ψ_i' and ψ_{*i} (as defined above), we arrive at

$$H_1\left\langle\frac{\overline{\partial u_1}}{\partial t}\right\rangle = 0$$

$$= W + \mathrm{RS}_1 + \mathrm{RT}_1 + \mathrm{IS} + \mathrm{IT} + D_1 \quad (26)$$

$$H_2\left\langle\frac{\overline{\partial u_2}}{\partial t}\right\rangle = 0$$

$$= \mathrm{RS}_2 + \mathrm{RT}_2 - \mathrm{IS} - \mathrm{IT} + D_2 + T + F \quad (27)$$

where the source and sink terms are (numbers refer to Fig. 4)

upper layer windstress [1]

$$W = \langle\bar{\tau}\rangle,$$

divergence of the Reynolds stress of the standing eddies [2]

$$\mathrm{RS}_i = H_i\left\langle J\left(\psi_{*i}, \frac{\partial\psi_{*i}}{\partial y}\right)\right\rangle$$

divergence of the Reynolds stress of the transient eddies [3]

$$\mathrm{RT}_i = H_i\left\langle\overline{J\left(\psi_i', \frac{\partial\psi_i'}{\partial y}\right)}\right\rangle$$

interfacial form stress due to the standing eddies [4]

$$\mathrm{IS} = -\frac{f_0^2}{g'}\left\langle\psi_{*1}\frac{\partial\psi_{*2}}{\partial x}\right\rangle,$$

interfacial form stress due to the transient eddies [5]

$$\mathrm{IT} = -\frac{f_0^2}{g'}\left\langle\overline{\psi_1'\frac{\partial\psi_2'}{\partial x}}\right\rangle,$$

horizontal momentum diffusion [6]

$$D_i = H_i A_4\left\langle\nabla^4\frac{\partial\psi_i}{\partial y}\right\rangle$$

mean topographic form stress [7]

$$T = -f_0\left\langle\psi_{*2}\frac{\partial B}{\partial x}\right\rangle$$

and bottom friction [8]

$$F = -H_2\epsilon\langle\overline{u_2}\rangle.$$

As examples, Fig. 4 displays the time and zonally averaged momentum balance for the cases FB and SC considered above. The left diagrams in Fig. 4 show the
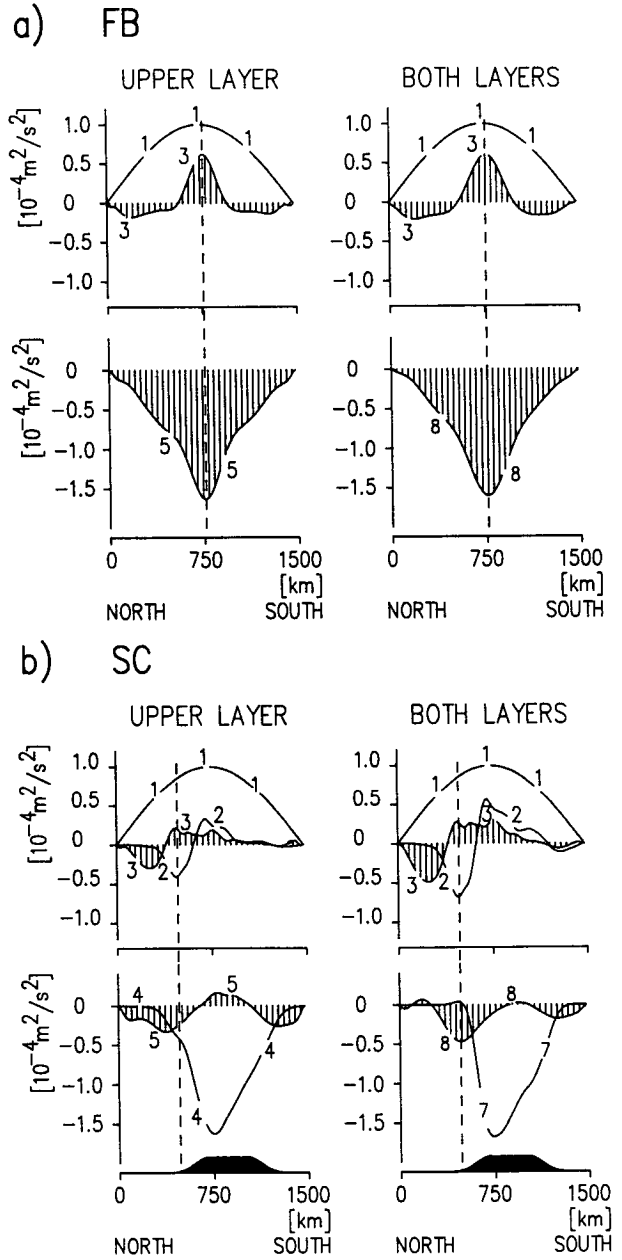

FIG. 4. Zonal and time-mean momentum balances as a function of latitude averaged over the last 11 years of integration (a) Case FB and (b) Case SC. The left panels show the upper layer balance and the right panels the barotropic momentum balance. The contributing terms are windstress [1], divergence of the Reynolds stresses of the standing [2] and transient [3] eddies, interfacial form stress due to standing [4] and transient [5] eddies, topographic form stress [7] and bottom friction [8]. The horizontal momentum diffusion term [6] is not shown because it is of $O(10^{-6}\ \mathrm{m}^2\ \mathrm{s}^{-2})$. The latitude of the highest zonally averaged time-mean zonal velocity (jet axis) is dashed and the zonally averaged topographic anomaly is indicated with an arbitrary amplitude in the lower panels of (b). Units are $10^{-4}\ \mathrm{m}^2\ \mathrm{s}^{-2}$.

meridional distribution of the terms that contribute significantly to the balance of the upper layer momentum $H_1\langle\overline{u_1}\rangle$ and the right diagrams are for the balance

of the barotropic momentum $H_1\langle\overline{u_1}\rangle + H_2\langle\overline{u_2}\rangle$. The abscisses runs from 0 km (northern boundary) to 1500 km (Antarctica) and the zonal mean topographic anomaly is sketched in the lower panels with a normalized amplitude. The axis of the mean zonal current is marked by a dashed line.

The source for the eastward momentum in the upper layer is the windstress [1] with a maximum amplitude in the middle of the channel. The divergence of the Reynolds stress of the eddies ([2] and [3]) redistributes zonal momentum in the horizontal direction. Interfacial form stresses ([4] and [5]) exchange momentum between the layers. Topographic form stress [7] and bottom friction [8] extract momentum from the system. Notice, however, that the form stresses can have both signs. Even the bottom friction may contribute to the forcing by the wind: only eastward bottom currents can act as a sink in a system forced by an eastward windstress, a westward current is a source of eastward momentum (e.g., close to the northern wall in case SC). The horizontal momentum diffusion [6] is not shown because it is one order of magnitude smaller than the smallest contribution.

The effect of the divergence of the Reynolds stress of the transient eddies [3] is to concentrate and intensify the time-mean zonal jet. In the flat bottom case FB eastward momentum is transported symmetrically from both flanks of the current into its center so that the current profile becomes sharper than the profile of the wind forcing (the current profile of the lower layer is reflected in the bottom friction [8]). The shape of the current and the momentum balance is in remarkable agreement with the parameterized zonal average models of Marshall (1981) and Ivchenko (1985).

The balance of the topographic case SC is considerably more complex. The symmetry is broken (this is only partly due to the uncentered mount, and the centered case C is only slightly more symmetric, with a more intense southern branch of the current in both layers). The current is on the northern flank of the seamount and eastward momentum is transported from its northern periphery to the jet center. This concentration of the current is due to the transient eddies [3]. The effect of the standing eddies [2], however, opposes the intensification of the jet, since they transport eastward momentum to the latitudes directly influenced by topography. The interfacial form stress due to the standing eddies [4] acts as the primary sink for the eastward momentum of the upper layer, whereas the interfacial form stress due to the transient eddies [5] plays only a secondary role as a sink of eastward momentum north and south of the bottom topography.

In the balance of the vertically integrated zonal momentum (right panels of Fig. 4b) the eddy Reynolds stresses play a similar role. The sinks for eastward momentum are now the topographic form stress [7] and the bottom friction [8]. The topographic form stress is by far dominating. It is of course concentrated over the topography while the bottom friction has its maximum effect along the axis of the jet.

We should emphasize again the fundamental difference of the above momentum balance to the more familiar condition for the basin circulation. In the channel the momentum input by the wind can only leave the fluid by transfer to the deep layer via interfacial form stress. Compared with basin conditions the momentum transfer to the deep ocean is very large: the flux of about 10^{-4} m^2 s^{-2} corresponds to a vertical eddy coefficient of $(10^{-4}$ m^2 $s^{-2})/(\Delta u/\Delta z) \approx 1$ m^2 s^{-1}, which exceeds the coefficients used in coarse resolution numerical models by two to three orders of magnitude. These small values are appropriate for a basin where the wind input can be balanced by net pressure gradients across the basin, i.e., flux of momentum through the lateral walls. With a lateral dimension $X = 4000$ km and a layer depth of 1000 m, the wind input of 10^{-4} m^2 s^{-2} would be balanced by a net pressure difference $(10^{-4}$ m^2 $s^{-2} \times 4000$ km)/ 1000 m $= 0.4$ m^2 s^{-2}, or equivalently, a 4 cm surface displacement across the basin. This is generally small compared to the pressure field associated with a Sverdrup circulation. For a basin the momentum flux to the deep ocean and consequently the bottom effects can thus be a negligible term in the momentum balance.

There is considerable evidence for a large vertical flux of momentum in the Southern Ocean. Indirect support comes from measurements of eddy heat flux. Using the geostrophic relation and expressing the interface displacement η by the corresponding perturbations of the temperature field T', the interfacial form stress may be related to the horizontal eddy heat flux

$$g\left\langle\overline{\eta\frac{\partial\zeta}{\partial x}}\right\rangle = f\langle\overline{\eta v_1'}\rangle \approx f\langle\overline{v_1'T'}\rangle\left(\overline{\frac{\partial\theta}{\partial z}}\right)^{-1} \quad (28)$$

where again ζ is the sea surface displacement, f is the Coriolis parameter, g is the gravity and θ is the potential temperature.

On the basis of this equivalence Johnson and Bryden (1989) obtain values in the range 1–8×10^{-4} m^2 s^{-2} for the Drake Passage, which exceeds the zonal average of the wind input. Equivalent vertical eddy viscosities are a few m^2 s^{-1}, which agree with the values found in the core of the ACC by the inverse model of Olbers and Wenzel (1989) based on hydrographic data.

4. Basic solutions for isolated topographies

The experiments with the different isolated topographies listed in Table 2 have been performed under otherwise identical conditions. They were all started from a state with no motion and integrated for 22 or 33 years, depending on the time span that was necessary to reach a quasi-steady state. The uncertainty in the mean values of the layer transports is about 1%–2% for the cases considered in this paper.

TABLE 2. Description of different experiments.

Case	Comments
FB	Flat bottom, externally disturbed after 11 years of integration
NC	Gaussian mount located north (+125 km) of central latitude
C	Meridionally centered Gaussian mount
SC	Gaussian mount located south (−125 km) of central latitude
HF	Topography as SC, but with higher bottom friction $\epsilon = 6 \times 10^{-7}$ s^{-1}
NB	Gaussian mount in contact with the northern boundary
SB	Same as NB but in contact with the southern boundary
BR	Blocking ridge from northern to southern boundary
D1	Combination of cases NB and SB, each tongue blocks ⅓ of the channel width
D2	As D1 but each tongue blocks ⅔ of the channel width
M1	Topography of the Macquarie-Ridge-Complex (see Fig. 13) rescaled to a maximum topographic anomaly amplitude of 500 m
M2	As M1 but with a maximum amplitude of 1500 m

See Fig. 8 for topographies of cases SC, NB, SB, D1, D2 and BR

The spinup to such a state generally took about 5 to 8 years. The mean transport in each layer and further bulk values characterizing the different solutions are given in Table 3. The general appearance of the solutions is discussed in the following section 4a. For the analysis of the momentum balance presented in section 4b we used the last 11 years of the integrations.

a. General spinup and flow patterns

1) CENTRAL TOPOGRAPHIES

The spinup of the flow is exemplified here with our basic experiment SC in Figs. 5a and 5b, showing (respectively) the time history of the transports and the total potential and kinetic energies in the two layers. The entire spinup has similarities to the analytic solution (16) for the spinup of the flat bottom case. The initial response of the water column to the onset of the wind is barotropic. This can be seen here in the ratio of the transports in the layers, reflecting the ratio of the mean layer thicknesses after roughly 5 months (i.e., $t = \lambda^{-1}$). In both layers, a meridional pressure gradient arises through a northward Ekman transport in the upper layer, which leads to a barotropic eastward geostrophic transport along the channel. The streamfunctions and interfaces during this phase are characterized by a smooth broad flow that in both layers reveals imprints of the topography (Fig. 6a). During this barotropic phase the meridional slope of the surface reaches 0.55 m across the channel (upward towards the north) while the slope of the interface between the layers is about 26 m (downward towards the north). Both slopes continue to increase approximately linearly over a couple of years. The potential energy thus reflects a parabolic increase. During this phase of baroclinic adjustment we notice considerable fluctuations in the kinetic energies and the layer transports. These fluctuations are associated with the barotropic instability of the developing jet. They are not visible in the potential energy since this mainly derives from the large-scale north–south slope of the interface.

During the baroclinic adjustment phase the channel flow builds up sufficiently strong velocity gradients to allow for the mechanisms of baroclinic instability. Baroclinic instability transforms available potential energy into kinetic energy around the scale of the internal Rossby radius of deformation, which is 32 km for the parameters under consideration. This instability process begins to act after the phase of relatively smooth increase of the baroclinic flow, as can be seen from the time series of the potential and kinetic energies. After about 8 years, the development of the potential energy

TABLE 3. Transports, energies and momentum balance. Transports ($\bar{T}_1$ and $\bar{T}_2$) and energies ($\bar{P}$, $\bar{K}_1$ and $\bar{K}_2$) are averaged over the last 11 years of each experiment. The momentum balance is described via area-integrated values of the following quantities: interfacial form stresses due to standing (IS) and transient (IT) eddies, topographic form stress (T) and bottom friction (F). These values are given as percentages of the integrated momentum input by the windstress. Negative values are an acceleration of the fluid in the direction of the windstress.

Case	$\bar{T}_1$ (10^6 m^3 s^{-1})	$\bar{T}_2$ (10^6 m^3 s^{-1})	$\bar{P}$ (m^3 s^{-2})	$\bar{K}_1$ (m^3 s^{-2})	$\bar{K}_2$ (m^3 s^{-2})	IS	IT	T	F
FB	377	982	724	65	97	0	100	0	100
NC	181	262	493	40	36	74	26	73	27
C	165	204	493	38	32	83	17	79	21
SC	168	198	507	40	33	84	16	79	21
HF	146	116	544	27	5	19	81	28	72
NB	278	664	608	53	74	30	70	34	66
SB	258	531	679	53	66	30	70	44	56
BR	84	−14	377	27	19	99	1	101	−1
D1	123	112	456	35	32	90	10	87	13
D2	73	−26	330	25	15	105	−5	103	−3
M1	132	69	657	40	30	93	7	92	8
M2	83	−31	561	31	15	107	−7	104	−4

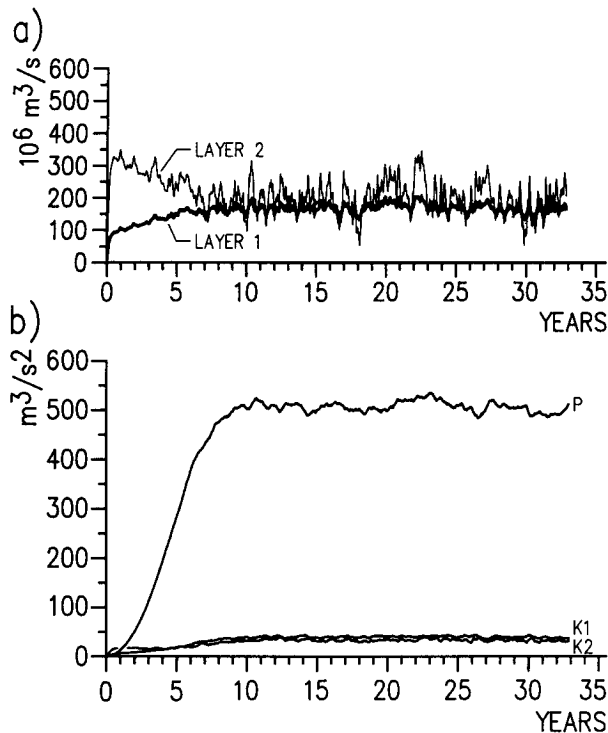FIG. 5. Case SC: Time development of (a) transports and (b) potential (P) and layer kinetic (K1, K2) energies. Units are Sv (10^6 m^3 s^{-1}) and m^3 s^{-2}, respectively.

changes from a smoothly increasing behavior into strong irregular oscillations with a quasi-steady mean. The kinetic energies begin to vary with higher amplitudes and on a higher level in both layers. Taking the necessary condition for baroclinic instability for the two layer model (e.g., see Kamenkovich et al. 1986)

$$u_1 - u_2 > \frac{\beta g' H_2}{f_0^2} \qquad (29)$$

and for simplicity the flat bottom solution (16), we find that baroclinic instability would start after

$$t \geqslant \beta H_2 / \tau_0 k^2 \approx 4 \text{ years} \qquad (30)$$

which fits with the described behavior of the system.

Figure 6b gives an impression of an instantaneous state of the flow during the fully turbulent phase. There is a discernable, mostly zonal jet flowing northward of the topographic barrier, which is strongly meandering and flanked by eddies on a scale of a few hundred kilometers. The jet width—even in the time-mean (see the mean zonal velocity profiles in Fig. 3)—is clearly smaller than the meridional scale of the wind. The surface and the interface show irregular deformations on the eddy scale but the location of the jet is still visible by a marked increase in the slope. The interface between the layers drops towards the north (roughly 750 m across the channel) and thus partly compensates the surface pressure. The mean deep transport is thus con-

siderably reduced in comparison to the barotropic initial phase (see Fig. 5a).

The experiments C and NC differ in their configuration from case SC only in a slight shift (125 km and 250 km, respectively) of the mount to the north. The southern jet and the entire channel (see Table 3) gains more transport but the general appearance of the flow is quite similar.

In the quasi-steady state of case SC the potential energy is roughly 10 times each of the kinetic energies in this state of quasi-stationary equilibrium. The kinetic energies of the two layers are of comparable magnitude and the jet in the upper layer is stronger than in the deep layer. The transports, however, show a reversed order. This also applies to the other cases with isolated topography (see Table 3). Notable exceptions—for obvious reasons—are case HF with the high bottom friction and the cases BR and D2 with substantial blocking effects of the topography in the deep layer (see below).

2) HIGH FRICTION

The increased bottom friction effects a decrease of the layer transports and a smoothing of the transport fluctuations. The mean transport in the lower layer is now even smaller than the transport in the upper layer. A further effect is a shortening of the barotropic time scale in agreement with the analytical solution (16). The time-mean streamfunctions for the upper layer and lower layer are shown in Fig. 7. The effect of increasing bottom friction is a broadening of the jet to a state of sluggish, quasi-homogeneous zonal flow. The southward deflection of the jet downstream of the topographic anomaly is increased but the standing wave pattern is diminished.

3) PARTIALLY AND TOTALLY BLOCKING RIDGES

The next series of experiments demonstrates the dependence of the flow pattern and the underlying dynamical balance on the shape of the topographic barriers. The basic case SC is supplemented here with the five additional topographies shown in Fig. 8. In case NB, the central Gaussian mount of the basic case is shifted northward to merge with the northern boundary and case SB is the southern counterpart. Notice that the meridional extent of the barriers and the unblocked passages are almost identical for the cases SC, SB and NB. In case BR, the deep layer is totally blocked by a ridge of 500 m height (notice that there are still 3500 m of unblocked water column in the deep layer). Cases D1 and D2 show two ridges extending from the northern and southern walls, blocking the flow along latitude circles. In D1 the individual tongues reach out over one-third of the channel width and in D2 they block two-thirds of the width. All cases were run with the low bottom friction value $\epsilon = 10^{-7}$ s^{-1} of case SC.

a)

b)
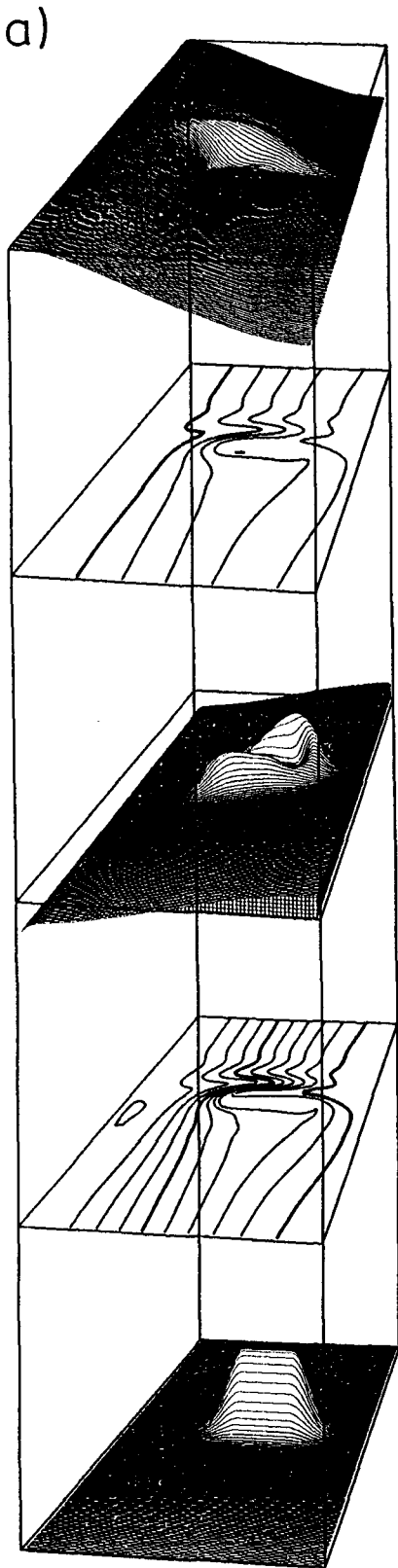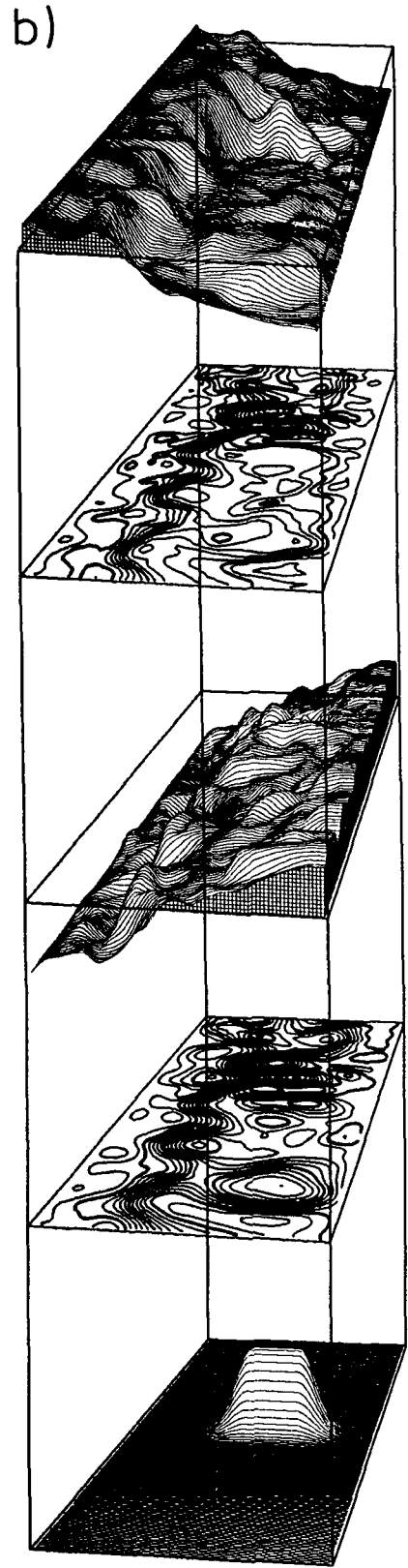
80 days

22 years

FIG. 6. Case SC: Streamfunctions and interfaces after (a) 80 days and (b) 22 years of integration. Shown are ζ, ψ_1, η, ψ_2 and B with arbitrary amplitudes and contour intervals from top to bottom and looking downstream.
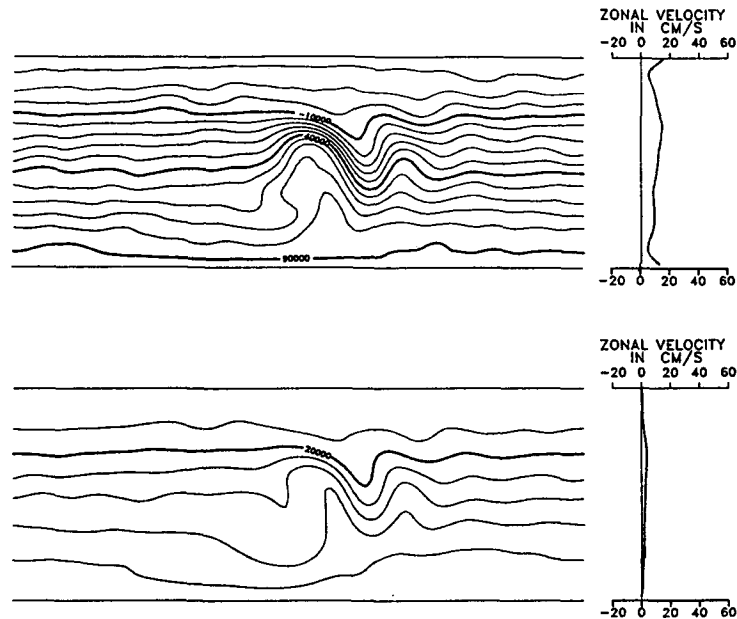
FIG. 7. Case HF: Time-mean streamfunctions and mean zonal velocities. Contour intervals are 10^4 m^2 s^{-1} in layer 1 (top) and 5×10^3 m^2 s^{-1} in layer 2 (bottom).

The time histories of transports for the cases NB, D1 and BR are shown in Fig. 9. These figures—as well as case SC—reveal a general feature of all experiments: the transients in transport are predominantly barotropic and hence determine the behavior of the fluctuations in the deep layer, even if the time-mean transport is small.

Concerning the magnitude of the mean transports and maximum velocities there is a clear ranking in the order NB, SB, SC, D1, BR and D2. The differences between these cases are by far larger than the difference to the case with the higher bottom friction presented above. The most remarkable feature appears in the totally blocked cases BR and D2, which have a westward transport in the deep layer. This agrees with the experiments of Treguier and McWilliams (1990) who also found westward deep jets in some experiments with centered seamounts and ridges. In their model, which has higher vertical resolution but smaller horizontal extent, these jets occur north and south from the windstress maximum and are mainly driven by the Reynolds stresses. Further discussion of deep westward transports is given in section 5d.

Figure 10 contrasts the patterns of the streamfunctions in the deep layer. The time-mean fields are displayed together with an instantaneous state at the end of each experiment. The cases NB and SB with the northern and southern topographic tongues reveal strong broad jets in both layers, centered just southward or northward on the flanks of the respective barriers. With increased blocking of the flow by the ridges, the deep circulation disintegrates into closed standing and

transient eddies. Two or even three standing eddies of alternating circulation appear in the lee of the ridges and are most pronounced in cases BR and D2. These cases with totally blocking topography allow only a rather sluggish upper layer flow with a broad scale upstream of the barrier. In all cases, the deep-layer circulation has developed closed gyres over the topography, which have a barotropic manifestation in the upper layer. This is more pronounced for NB and D1. The reason for closed barotropic circulation over northern ridges can be found in the closed planetary vorticity contours f/H, which appear in all cases with ridges at the northern boundary. The topographically
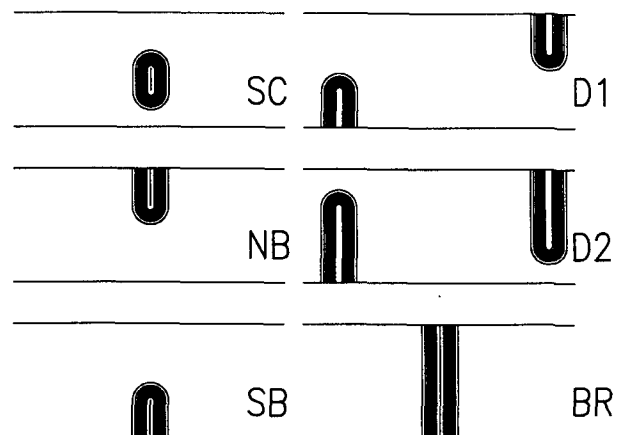

FIG. 8. Bottom topographies of cases SC, NB, SB, D1, D2 and BR (see Table 2). Contour intervals are 50 m ranging from 0 to 500 m.
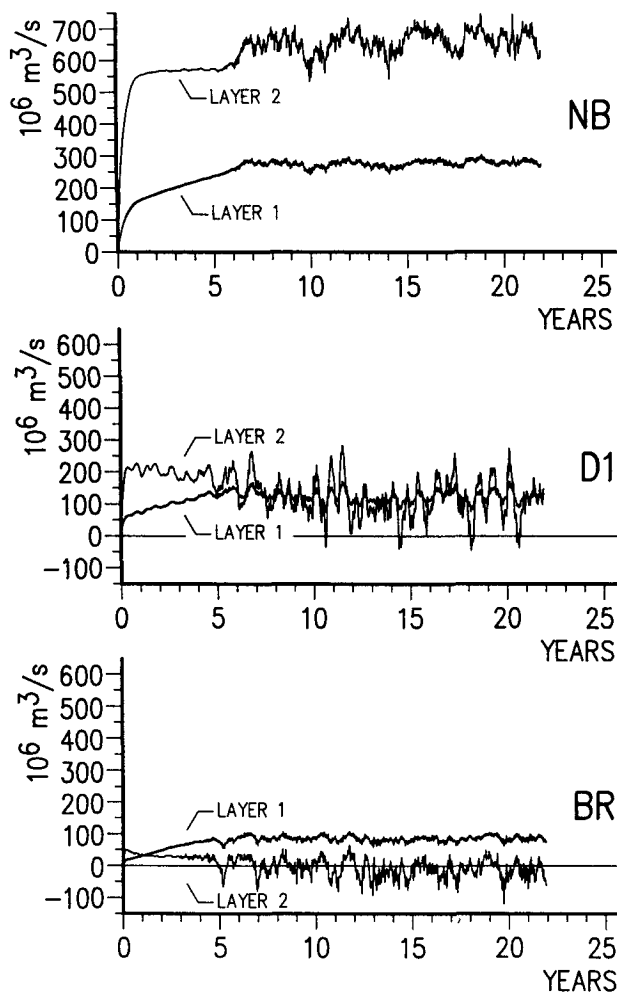
FIG. 9. Time series of layer transports in units of Sv
of cases NB, D1 and BR (top to bottom).

induced stationary lee waves have a larger scale compared with the cases SC and HF.

4) EDDY PROPERTIES

We would like to point out a few basic properties of the eddy field, some of which were also found by McWilliams et al. (1978) in their smaller dimensioned channel experiments and McWilliams and Chow (1981) in their flat bottom experiments. Some instantaneous eddy streamfunctions are displayed in Fig. 11. Case SC can be taken as typical for the rest of the experiments with isolated topographies and low bottom friction.

The eddies have a substantial barotropic component but in all experiments the eddy scale in the lower layer is substantially larger than the eddy scale in the upper layer (so there are more eddies here than in the bottom layer). The eddy diameter in FB is roughly 250 km in the upper layer and 350 km in the lower layer, the

corresponding values in SC are 300 and 380 km and in HF 200 and 320 km, respectively. This fairly obvious scale difference between the layers cannot be explained by linear instability theory. Additionally, linear theory cannot account for the difference between the cases with high and low bottom friction, since in both experiments (SC and HF) the vertical current shear is almost the same and the scale range of linearly unstable modes should thus be equal.

Case FB reveals a property that may explain the countergradient transport of momentum of the transient eddy field in almost all of the experiments. Eddies northward of the current are tilted from northwest to southeast, whereas the eddies south of the current are tilted from southwest to northeast. Obviously, in both configurations the correlation $\overline{u'v'}$ is such as to transport zonal momentum into the central jet. The tilted eddy shape, in turn, is due to the reduction of the intrinsic Rossby wave phase speed by this central current (McWilliams and Chow 1981).

The eddy kinetic energy is generally larger in the lee of the topographic obstacles. Since there is no direct source of mean eddy kinetic energy due to the interaction with the bottom (e.g., see McWilliams et al. 1978) the enhancement behind the topography must be an indirect effect. It may in fact be associated with the acceleration of the mean flow in the lee of the topography.

b. Momentum balance

The momentum balance of our standard case SC was presented in section 3 (see Fig. 4b). Here we will highlight the basic differences among the experiments with isolated topographies. We confine our discussion to the cases HF, NB, D1 and BR. The time and zonally averaged momentum balance for these cases is shown in Fig. 12. The balances of the cases C and NC are very similar to SC and the couple NB and SB are almost symmetrical with respect to the midlatitude of the channel. Also, case D2 and BR show no fundamental difference in the zonally averaged balance (though they differ of course in the streamfunction pattern, see Fig. 10).

1) HIGH FRICTION

The divergences of the Reynolds stress of the eddies in case HF have the same structure as in the basic case SC but with greatly reduced amplitudes. The most important difference between the small friction and high friction states appears in the role of the interfacial and topographic form stress terms. In case HF, the eastward upper layer momentum is predominantly transferred to the deep layer by the interfacial form stress due to the transient eddies. This is in contrast to the small friction case where the standing eddy interfacial form stress served as the major sink (see Fig. 4b). This originates from the greatly reduced standing wave pattern
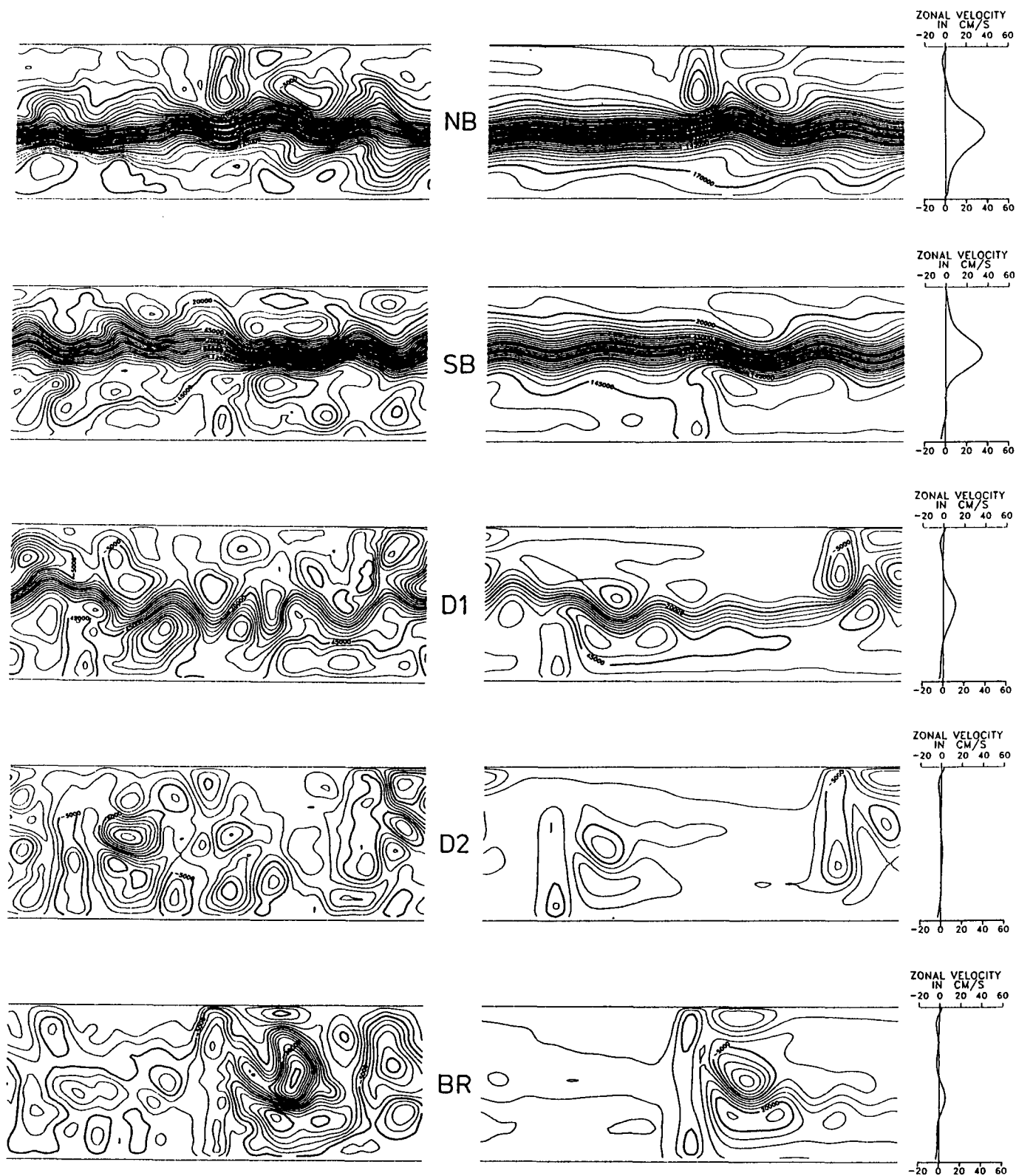
FIG. 10. Instantaneous (left) and time-mean (right) streamfunctions in the lower layer of cases NB, SB, D1, D2 and BR. Contour intervals are 5×10^3 m^2 s^{-1}.
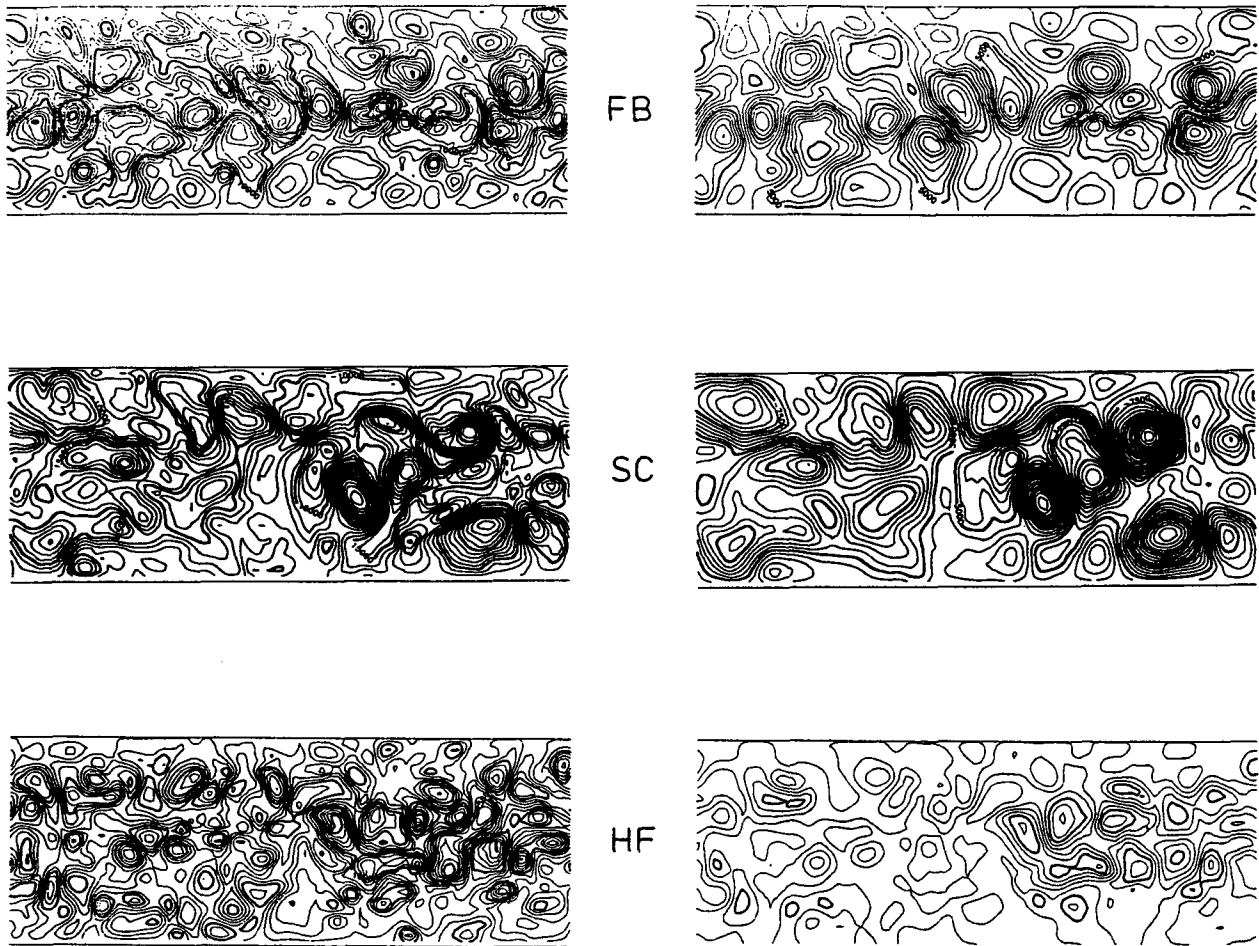
FIG. 11. Instantaneous eddy streamfunctions ψ_i' at the end of the integrations of cases FB, SC, and HF (from top to bottom). Upper layer fields left and lower layer fields right. Upper layer: CI = 5 × 10³ m² s⁻¹. Lower layer: CI = 2.5 × 10³ m² s⁻¹.

in case HF (see Fig. 7). There is also a remarkable difference between the relative role of friction and topographic form stress in the barotropic balances of the two cases. Although the velocities are much smaller in case HF, the bottom friction acts here as the major sink for the eastward momentum. The broad sluggish flow is apparently unable to support significant bottom pressure gradients across the topography. This can be directly inferred by comparison of Figs. 3 and 7.

2) PARTIALLY AND TOTALLY BLOCKING RIDGES

The downward flux of momentum out of the upper layer is generally carried by the transient eddies in the free passage part of the channel and by the standing eddies in the blocked part. The reason is obviously the development of standing eddies predominantly in the lee of the barriers while moving eddies can find their path easier over the free passages. This explains the differences between cases SC and BR, where the effect of the standing eddies dominates, and the cases NB

and SB, where the transient eddies carry most of the interfacial form stress. In all cases the upper layer jet is concentrated and intensified by the Reynolds stress due to transient eddies. The opposing effect of the standing eddy stress, which was present in case SC, is diminished and even reversed for the totally blocked case BR.

Since lateral momentum transport by the Reynolds stresses is small the barotropic balance is dominated by bottom friction over the free flow area while topographic form stress takes over in blocked areas. The cases NB and SB with the northern and southern topographic tongues appear to be highly governed by the bottom friction and the large transport in these solutions may thus be attributed to the low friction parameter acting in the broad free passage of these experiments. There are clear remnants of this feature in case D1. The cases SC and BR (as well as D2) obtain their structure predominantly from the topographic form stress. In all cases the transient eddies converge barotropic momentum to the jet axis on the flank of the
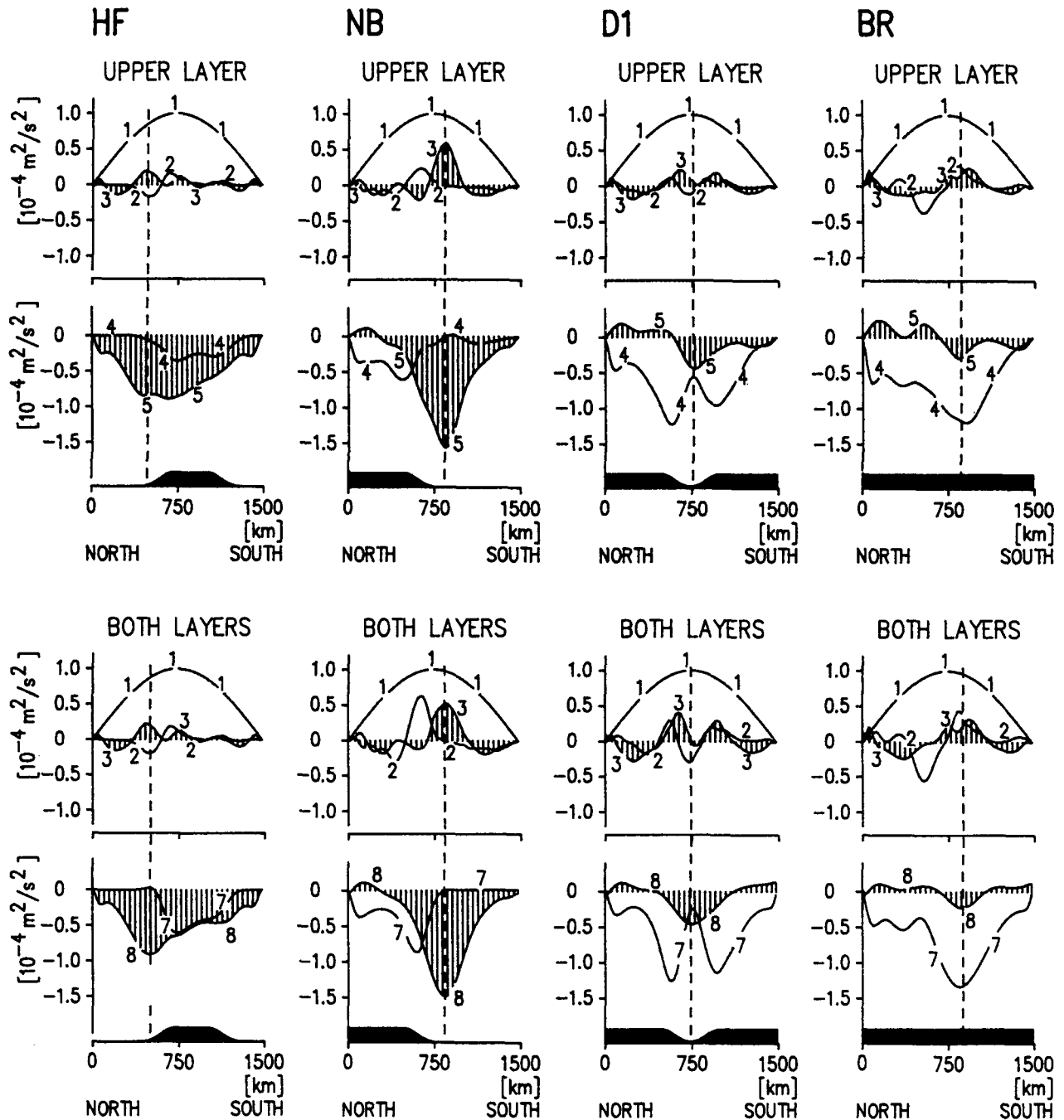
FIG. 12. Same as Fig. 4 for cases HF, NB, D1 and BR, except that the top panels show the upper layer momentum balance and the bottom panels, the barotropic momentum balance.

barrier, while the standing eddies have their maximum convergence more uphill to feed the sink by topographic form stress.

Values for the total area integrated form stresses and the bottom friction can be found in Table 3. These clearly reflect the different role of transient and standing eddies in the experiments and their dependence on the environment: friction as well as unblocked flow severely

reduce the standing eddy pattern so that the downward flux of momentum must be accomplished by the transients. At the same time—since the topographic form stress is entirely sustained by the standing eddy field—bottom friction must take over in the balance of the flow in the deep layer.

Finally we should like to point out that (with the minor exception of the blocked cases BR and D2) the

sum of all net form stresses and the frictional stress are positive; their net effect for an eastward forced flow is a downward transport of eastward momentum through the water column and through the ocean floor. This is by no means mandatory (BR and D2 are examples where friction with reversed bottom velocities accelerates the eastward flow at a small rate) nor trivial. We know from experiments with primitive equation models that the topographic form stress can support the wind in supplying eastward momentum (e.g., Gill and Bryan 1971).

5. Flow over realistic topography: The Macquarie Ridge experiments

The flow regimes in our channel model bear many similarities with the circumpolar current but the applicability of our results to the ACC may be questioned for many reasons. There is the obvious discrepancy in the scales of our channel and the circumpolar region. The model results can only give a typical or, in some sense, average picture of the actual current. The other discrepancy is the extreme simplicity of the topographies used in the experiments. These were smooth isolated mounts or ridges, which in many of the cases, leave more or less broad passages for the currents to find a path through the channel without seeing much of the topography. Nevertheless, the zonal symmetry is generally broken and the study of the momentum budget clearly indicates that the flows are considerably affected by the topography. A further unsatisfactory point is the arbitrary vertical extent of the topography. A mount of 1000 m height would not violate the QG-scaling, but would it be more appropriate?

Some of these points are addressed in this section. We present the two experiments—M1 and M2 (see Table 2)—which use a rescaled form of the highly resolved bathymetry of the Macquarie Ridge area as the topography in the otherwise unchanged QG-channel. The bathymetric data are from the $\frac{1}{12}$ degree global topography Digital Bathymetric Data Base 5 (DBDB5) dataset distributed by the U.S. National Geophysical Center in Boulder, Colorado.

a. The oceanographic environment and set-up of the model

The Macquarie Ridge Complex is a narrow ridge and trench system extending for about 1000 km between 50° to 60°S immediately southwest of New Zealand. It is cut by three deep passages (the major one is at 56°S) and partly bounded to the east and west by deep trenches. To the south it falls off to a relatively deep ocean region and farther south, at about 60°S, it merges with the Southeast Indian Ridge. The bathymetry of the area is shown in Fig. 13 on the grid used in the channel experiments M1 and M2. To achieve the periodicity of the model the bathymetry has been linearly interpolated over 10 gridpoints (i.e., a 200 km region on the left-hand side of the channel). The convergence of the meridians has been neglected. Apart from the outstanding Macquarie Ridge, the Campbell Plateau extends from the northern wall over a quarter of the channel width, and the relatively rough midocean ridge runs diagonally through the channel. East and west of this feature there is a smooth, deep ocean basin that merges with the Australian–Antarctic Basin in the west and the Southwest Pacific Basin in the east. The more or less zonal topography at the southern boundary in the western half of the channel is the continental rise of Antarctica.

We have chosen this region for two reasons. First, on the large scale, there is a strong guidance of the ACC by the midocean ridge system (see Fig. 14), as is seen in the dynamic topography (Gordon et al. 1978; Lutjeharms 1982; Reid 1986).
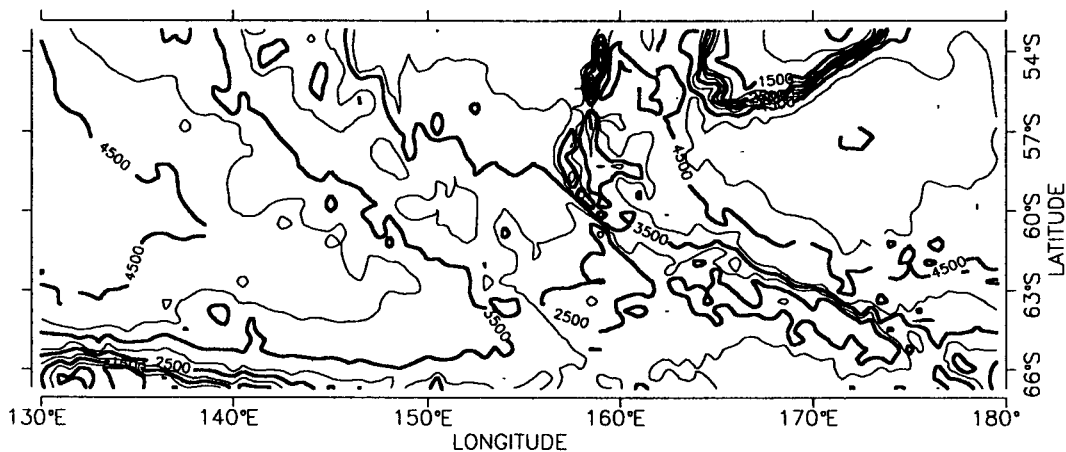
This large-scale ridge system shifts between 140°E

FIG. 13. Topography for the Macquarie Ridge Complex experiments (CI = 500 m). This topography is rescaled for the M1 and M2 experiments (to maximum amplitudes of 500 m and 1500 m, respectively) to account for the restrictions of the quasi-geostrophic approximation.
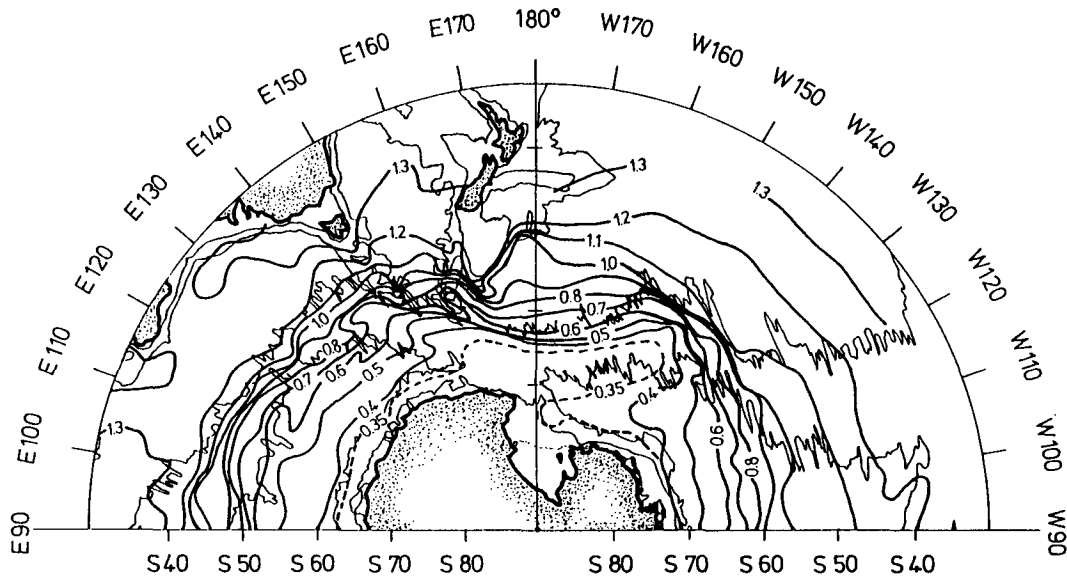
FIG. 14. Dynamic topography 0/1000 db from Gordon et al. (1978). CI = 0.1 m.
Contour of depth 4000 m is shown by light lines.

and the Macquarie area (at about 160°E) by more than 1000 km to the south. The main stream of the ACC, however, only partly follows the topography when entering the Macquarie area (cf. also Gordon 1972; Patterson 1985). The stream splits, and a northern branch crosses the passages in the Macquarie Ridge and focuses in a current flowing on the eastern side of the Campbell Plateau. A southern branch follows the midocean ridges around the southern tip of the Macquarie Ridge to continue in a strongly guided stream along the northern flank of the Pacific–Antarctic Ridge. A part of this stream is fed from water flowing out of the South Indian Abyssal Plain from the west.

A second and more relevant reason for selecting this region is found in the high mesoscale variability of the area. Maps of the sea height variability or eddy kinetic energy obtained from satellite altimetry (Cheney et al. 1983; Patterson 1985; Daniault and Ménard 1985; Koblinsky 1988) show a series of maxima along the path of the ACC that are either associated with western boundary currents or appear highly correlated with the passage of the ACC over submarine topographic features. The maximum in the Macquarie area is outstanding among the latter class. On the basis of the *Eltanin* hydrographic surveys of the region, Gordon (1972) speculated that the interaction of the ACC with the Macquarie Ridge leads to eddy shedding from this topographic feature. Boyer and Guala (1972) made an attempt to model this process with a laboratory and a theoretical model based on the barotropic vorticity equation. Convincing evidence for these eddies behind the gap in the ridge was later found in SEASAT data by Colton and Chase (1983) and in GEOSAT data (e.g., see Chelton et al. 1990).

The topography shown in Fig. 13 has depth variations that are beyond the applicability of QG dynamics. It was, therefore, scaled to a maximum of 500 m in case M1 and 1500 m in M2. The wind forcing and the friction parameters were those of the standard case SC.

b. Spinup and circulation

The model is of course far too simple to simulate the full details of the above-described circulation. The major hindrance arises from the imposed constraint of periodicity and the solid walls that prevent the correct inflow conditions at the west. Nevertheless, the experiments M1 and M2 reveal some of the observed oceanographic features.

The spinup of flow over the complex topography is similar to the cases with isolated topographies (Fig. 15 displays the spinup of case M2). A marked difference is found in the temporal behavior of this state: the potential energy shows erratic fluctuations with large amplitudes and periods of several years. The experiments M1 and M2 were therefore integrated for the longer time span of 33 years, which still appears only marginally sufficient to perform adequate time averaging.

Figures 16 and 17 show instantaneous eddy streamfunctions and time-mean streamfunctions of the two cases M1 and M2. There are many similarities as well as dissimilarities between these simulations and the observations. In both experiments, the upper-layer circulation is concentrated in a strong jet situated on the northern flank of the midocean ridge running diagonally across the channel. Because of the periodicity the jet has to reenter the channel on the western side far to the south, where it clings to the continental rise.
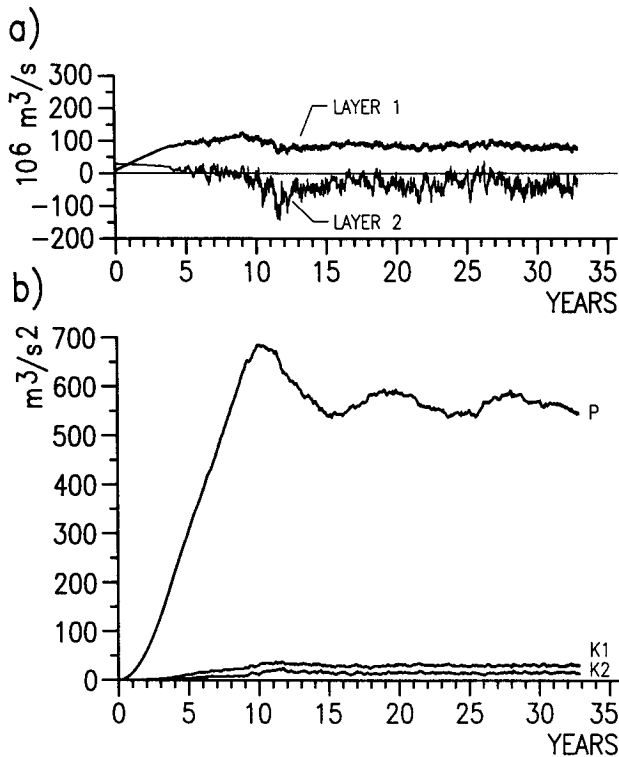
a)

b)

FIG. 15. Case M2: Time development of (a) transports and (b) potential (P) and layer kinetic (K1, K2) energies. Units are Sv (10^6 m^3 s^{-1}) and m^3 s^{-2}, respectively.

After impinging on the midocean ridge, there is a marked shift to the north in correspondence to the approximate conservation of potential vorticity. At this point a part of the flow separates and proceeds zonally as a secondary southern jet. After a northward excursion when passing the midocean ridge, this secondary jet partly rejoins the main current. This general pattern, which is sharply concentrated in the high topography case M2 and more washed out in the low topography case M1, shows fair agreement with the 0/1000 db dynamic topographies of Gordon et al. (1978, see Fig. 14) and Reid (1986). According to the dynamic topography the diagonal jet comes from latitudes north of the model domain. This is inhibited in the model due to the solid wall, and therefore must be fed from the southerly entry. The main disagreement is the total absence of the current on the eastern flank of the Campbell Plateau, an outstanding feature in the dynamic topography. This feature is not evident in the model simulations.

The two cases show other interesting differences in the circulation pattern in the Macquarie Ridge area. In the low topography case M1 the instantaneous (as well as the mean) jet passes with southward excursion in a broad flow over the ridge south of 58°S. There are large closed cells in the deep mean circulation to the south and to the north of the jet in the deep basins,

which partly extend over the ridge. In the high topography case M2 the jet does not dip as far to the south but passes right through the 56°S passage in the Macquarie Ridge system after a northward excursion. The southern part of the ridge seems now high enough to exert a substantial blocking effect. The deep cells have disappeared or are greatly reduced in their sizes.

Is there any eddy shedding from the Macquarie Ridge? Figures 16 and 17 show an instantaneous view of the transient eddies for both layers. There are eddies all along the path of the jet, with significantly smaller scales in M2 than in M1 and the cases with isolated topography. Again, the eddy signal is highly barotropic and the average size is smaller in the upper layer. Since M1 and M2 are otherwise identical in the external parameters, the smaller eddy size in M2 must be generated by the higher topography of this experiment. The larger the amplitude of the hills and valleys the more the flow is forced to adjust to the bottom structure on the corresponding spatial scale.

Extrapolating our results from the experiments with isolated topographies, we can identify the series of hills on the northern part of the diagonal midocean ridge as one likely source of topographically generated eddies. This circulation feature is similar to the case NB, which has a ridge extending southward from the northern wall. In the three cases, NB, M1 and M2, there is a standing eddy dipole immediately behind this ridge, particularly in the deep layer, and transient eddies traveling downstream. Directly behind the Macquarie Ridge, however, the transient eddy signal diminishes and only begins to increase when the jet approaches its southern most position in the deep basin of the model. This behavior is indeed a permanent property, as is shown by the maps of the mean eddy kinetic energy displayed in Fig. 18.

c. Momentum and vorticity balance

The momentum balances of the Macquarie Ridge experiments are displayed in Fig. 19. Though the principal dynamical relations are fairly similar to the isolated topography cases (Fig. 4 and 12), a closer inspection reveals a higher degree of structural complexity, at least for the high topography case M2. All internal components of the balance show considerable variations on a scale of about 100 km. This feature is in qualitative agreement with the experiments of Treguier and McWilliams (1990), who used random topography with different average scales in a multilayer QG-channel. The same authors also found that some components are highly correlated on the small scales. They obtained a negative correlation between the total Reynolds stresses (RS + RT) in the lowest layer and the topographic form stress T. Our experiments indicate small scale correlations in all internal components. These are entirely associated with the standing eddy field: the RS in both layers are negatively correlated
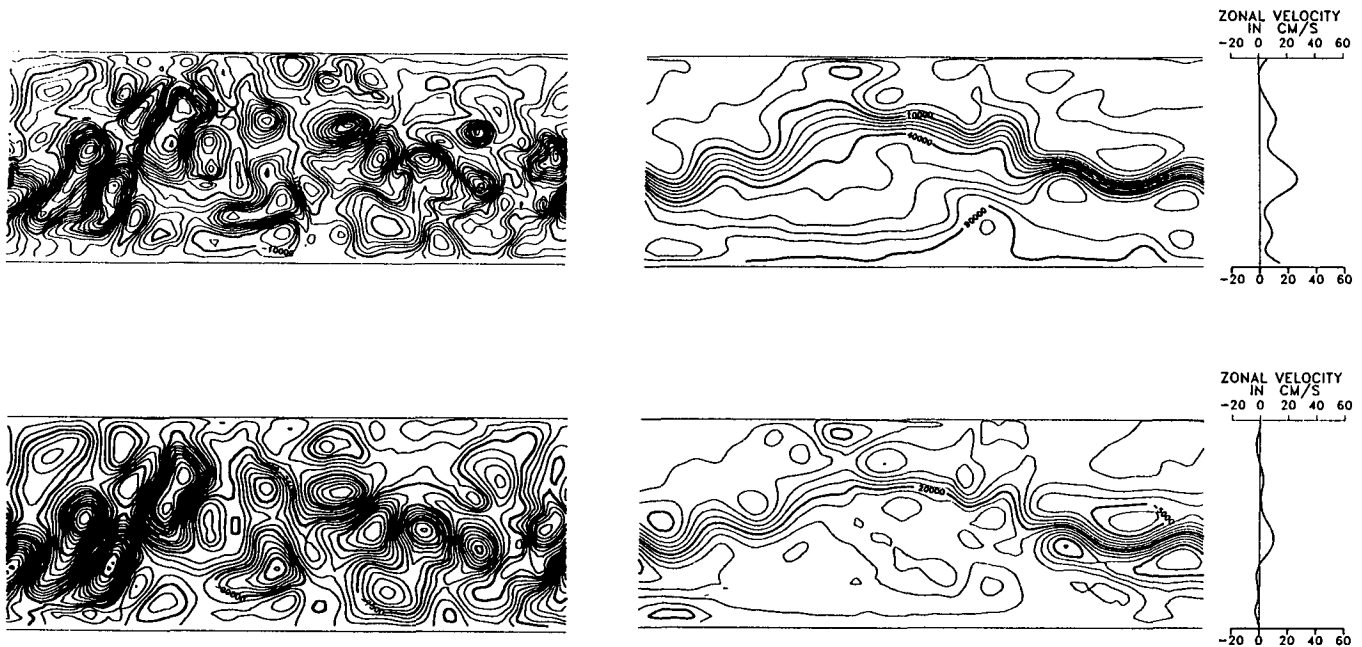
FIG. 16. Case M1: Instantaneous eddy streamfunctions after 33 years of integration (left), time-mean streamfunctions (averaged from 22 to 33 years) with the time and zonal mean zonal velocity distribution (right). Top row shows the upper layer and bottom row the lower layer fields. Upper layers: CI $= 10^4$ m^2 s^{-1}. Lower layers: CI $= 5 \times 10^3$ m^2 s^{-1}. Velocities are in cm s^{-1}.

with IS and T, and the latter two components are in phase. Furthermore, all correlations are stronger when bottom friction effects are small. Notice that the high topography case M2 presents a practically frictionless flow regime. Friction plays only a 4% role in the total balance of M2 (see Table 3).

Treguier and McWilliams (1990) argue on the basis of a negative areal correlation between the relative vorticity $\nabla^2 \psi_*$ and the topography B in the deepest layer of their experiments that the Reynolds stress RS + RT in the deep layer should equal the negative topographic form stress T. They support the negative correlation
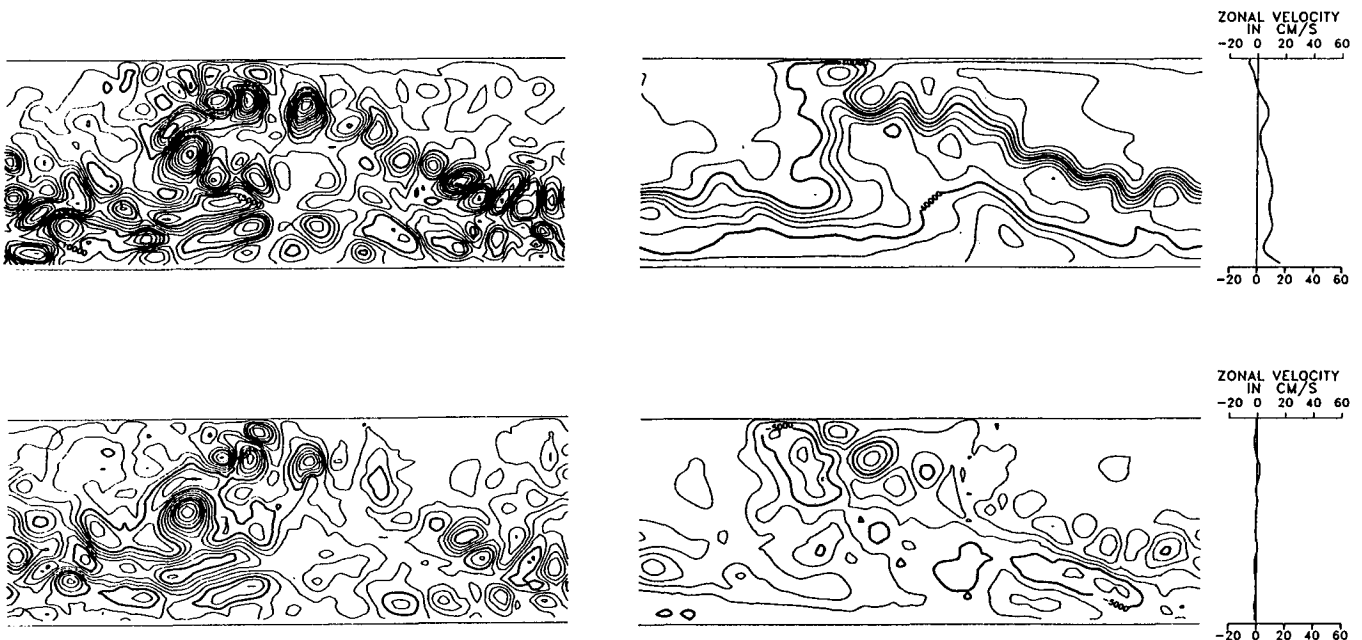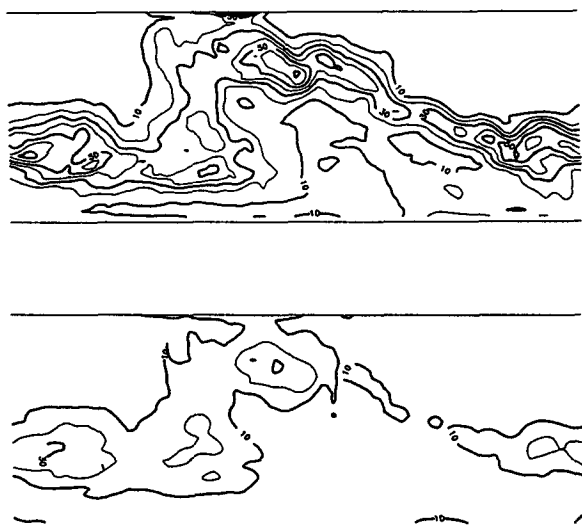

FIG. 17. As in Fig. 16 for case M2.

FIG. 18. Case M2: Time-mean eddy kinetic energies.
Top: layer 1, and bottom: layer 2. CI = 10 m^3 s^{-2}.

eddy transport of potential vorticity must thus be small compared to the mean advection terms in the balance:

$$J(\overline{\psi_1}, \overline{q_1}) = \frac{1}{H_1} \mathrm{curl}\tau - J(\overline{\psi_1', q_1'}) - A_4\nabla^6\overline{\psi_1}. \quad (33)$$

The zonal average of (33) was analyzed by McWilliams et al. (1978) for a smaller channel with a Gaussian hill. They found indeed a dominance of the standing eddy

between $\nabla^2\psi_*$ and B, which is observed in their model, by the functional relation between the potential vorticity and streamfunction

$$H\nabla^2\overline{\psi} + f_0B + H\beta y = G(\overline{\psi}), \quad (31)$$

which applies to a barotropic unforced inviscid flow. Treguier and McWilliams argue that for a linear functional G and for small scales, (31) implies

$$\nabla^2\psi_* \approx -\left(\frac{f_0}{H}\right)B. \quad (32)$$

This results immediately in RS $\approx -T$ using the definitions following Eqs. (26) and (27). Of course, the validity of this relation is considered on the small scales only. On large scales, the net RS vanishes whereas the net T must balance the net interfacial form stress and bottom friction.

Our results suggest that the correlation structure is directly related to the almost frictionless state of the channel flow. Figure 20 shows the scatter diagrams of potential vorticity and streamfunction fields for both layers of case M2. The figures show the relations for the time-mean, the standing eddy part, and the transient eddy part.

Surprisingly, there is a strong correlation between the potential vorticity and the streamfunction in the upper layer, though this is directly forced by the wind. The figures indicate an almost linear relation for the time-mean and the standing eddy part, while the transient eddy part appears more scattered. The friction effects (wind forcing and horizontal diffusion) and the
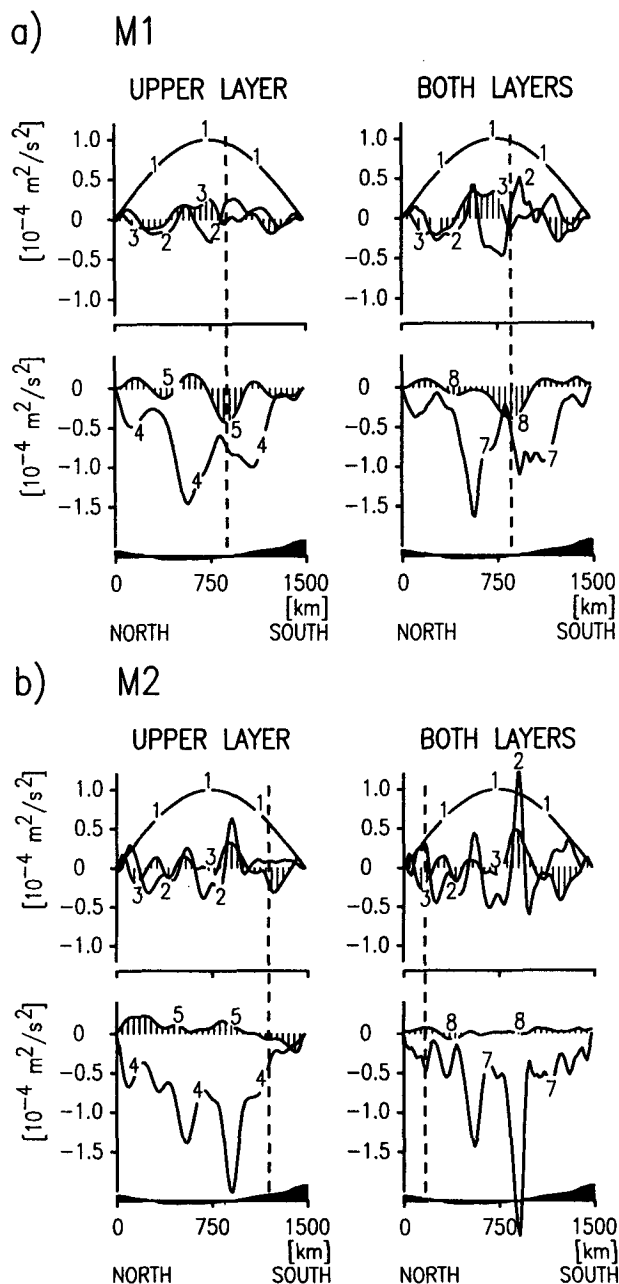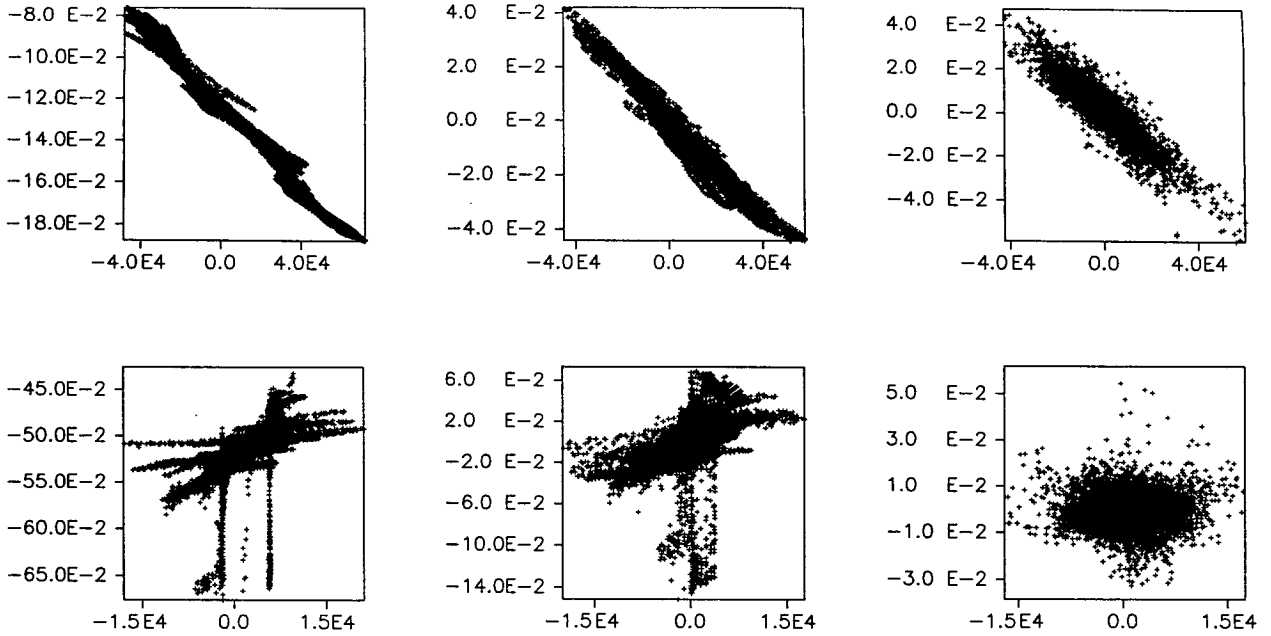

FIG. 19. As in Fig. 4 for (a) case M1 and (b) case M2.

FIG. 20. Case M2: Scatter diagrams of potential vorticity (y-axis) against streamfunction (x-axis). Left to right: time-mean, standing and transient fields. Top row: upper layer, and bottom row: lower layer. Units are m s^{-1} for the potential vorticity (due to a multiplication with the squared mean layer thicknesses) and m^2 s^{-1} for the streamfunctions.

terms [arising from the left-hand side of (33)] over the friction and transient eddy terms in the latitudes of the mean jet. From

$$\overline{q_1} = G(\overline{\psi_1}) \qquad (34)$$

we find immediately

$$RS_1 = -IS \qquad (35)$$

by multiplying (34) by $\overline{v_1} = \partial\overline{\psi_1}/\partial x$ and zonal integration. This explains the observed negative correlation of these quantities on small scales.

In the lower layer we see a more complex picture. The transient part is much more uncorrelated whereas the time-mean fields reveal a superposition of different, more or less linear, correlation patterns (the vertical lines derive from the constant values of the streamfunction and the variation of the topographic potential vorticity contribution on the lateral boundaries). Such structures in the $q(\psi)$-scatter plot were first found by Bretherton and Haidvogel (1976). These separate relations are associated with the closed circulation cells in the lower layer visible in Fig. 17. A functional relation

$$\overline{q_2} = G_n(\overline{\psi_2}) \qquad (36)$$

in each cell n implies that the momentum balance is almost closed for the standing eddy part: multiplying this relation by $\overline{v_2} = \partial\overline{\psi_2}/\partial x$ we obtain

$$IS + RS_2 - T = 0. \qquad (37)$$

Apparently, a small scale structure in any of the con-

tributions in (35) and (37) (most likely the Reynolds stresses RS) must be reflected in the remaining terms of the balance and cause the observed correlation structure. Notice that for large scales [larger than $(g'H_2/f_0)^{1/2}$ and $(|\partial G/\partial\psi_2|)^{1/2}$] (36) yields the large scale balance

$$IS = T \qquad (38)$$

in the zonal mean.

d. Deep westward transports

The deep flow in M1 (Fig. 16) appears as a barotropic extension of the upper layer flow, as in the cases with isolated topography (except the highly blocked cases). In M2, however, the deep circulation is entirely broken up into eddies (Fig. 17). In both cases M1 and M2 there is a series of westward currents in the deep layer in the zonal mean. In M1 these are compensated by the eastward jet in the center to give a net eastward transport but M2 shows a westward transport. There is similarity with the blocked experiments D2 and BR (see Fig. 10).

The driving force of these deep westward currents is not evident. As pointed out in the previous section there is a high spatial correlation in the zonal mean between the standing eddy contributions to the interfacial form stress and the Reynolds stress and also the topographic form stress. All these stresses are also correlated with the zonal current in the deep layer, in particular there is a positive correlation between $\langle\overline{u_2}\rangle$ and the topographic form stress T (this is visible in curves

[7] and [8] of Fig. 19; notice that the bottom friction [8] displays $-\langle \overline{u_2} \rangle$. At first sight it appears plausible that the westward stress T drives the deep westward jets in $\langle \overline{u_2} \rangle$ in an overcompensation of the wind input and the interfacial downward momentum flux. The question of driving agent of these deep jets, however, cannot be answered strictly from the time-mean balance. A detailed investigation of the time-mean evolution of the momentum balance under a perturbed forcing is required but beyond our computer resources.

If the momentum balance is integrated not only zonally but over the entire channel depth and area, the Reynolds stresses vanish and we obtain (23) or, with consideration of the time rate of change

$$\left(\frac{\partial}{\partial t} + \epsilon \right) \int_0^Y \langle d_2 u_2 \rangle dy$$

$$= \int_0^Y \left(\langle \tau \rangle + \left\langle B \frac{\partial p_2}{\partial x} \right\rangle \right) dy. \quad (39)$$

It is evident from this equation that total westward momentum or transport can only be generated—in case of eastward windstress—by the topographic form stress. Holloway (1987) has shown that the net topographic form stress for a barotropic flow over random topography consists of a drag part (i.e., opposing the mean flow) and a second part, which is negative (i.e., propelling the fluid westward) over a wide range of circumstances (in particular negative transports). It is likely that we have in these Macquarie Ridge experiments a manifestation of Holloway's theory.

6. Summary and conclusions

The balance of the zonal momentum in the eddy-resolving quasi-geostrophic channel found by Mc-Williams et al. (1978) is quite robust to moderate changes of the value controlling the bottom friction and to changes of the channel topography. The input of eastward momentum by the windstress is transferred vertically by interfacial form stress to the bottom layer, and leaves the system through the action of bottom friction in the flat bottom part of the channel and by form stress against the topography in the blocked latitudes. The interfacial form stress is set up by the eddies. Depending on the location of the topographic barriers in the channel and the value of the bottom friction, either transient or standing eddies dominate in the lee of the topography and carry the main contribution to the interfacial form stress. The main sink of the momentum in the deep layer and the barotropic momentum is the topographic form stress, unless the frictional parameter is very high or the topographic obstacles are far away from the latitudes with the highest winds. Lateral stresses due to the eddies may transport momentum up the gradient to the center of the jet, quite in contrast to diffusive parameterizations.

Our experiments with realistic topography filling the entire channel—the Macquarie Ridge cases—sum up the properties found in the experiments with isolated topographic obstacles. The case with the high topography of the area (scaled to a maximum of 1500 m) represents an almost frictionless model of a zonal channel flow. The interfacial form stress is mainly caused by standing eddies. This is in contrast to the recent analytical model of the ACC by Johnson and Bryden (1989) who parameterized the vertical momentum transport entirely in terms of the equivalent lateral heat flux contribution from baroclinically generated transient eddies.

The above balance of the zonal momentum has been proposed by Munk and Palmén (1951) to govern the flow of the Antarctic Circumpolar Current. Do these eddy resolving experiments give us further insight into the momentum balance of the ACC or even prove that the topographic form stress is important in this current?

In the light of the eddy resolving experiments the simulations of the ACC in coarse global circulation models appear highly questionable. In these models, the wind input is generally balanced by lateral diffusion of zonal momentum into the adjacent ocean basins or to the boundaries. Vertical momentum transport is negligible and the topographic form stress is a source of eastward momentum. All these properties disagree with the eddy resolving models.

Since observations show the presence of a strong eddy field in the ACC, it is very likely that these eddies act in the real ACC as in the eddy resolving model, and that diffusive parameterizations of eddy transports may introduce errors. There are indications in the inverse model of Olbers and Wenzel (1989) that the vertical momentum transport in the ACC is as high as the wind input. Again, it is likely that such a high flux is associated with the eddies and that interfacial form stress is the probable mechanism. The observed magnitude of lateral eddy heat transport values (see Bryden 1983, for a review) also support an extremely large vertical momentum transport in the ACC.

Although the eddy resolving model described here (as well as the one of McWilliams et al. 1978) possesses many degrees of freedom to establish a particular realization of the mean current in the channel (much more than a coarse global circulation model), the overall balance of the momentum is of course severely constrained by the model set-up. Since there are no lateral stresses at the walls, there is no other way for the momentum to leave the channel than via the bottom. In the quasi-stationary state the net stress on the interface must therefore be as large as the imposed windstress and the eddies must find a way to achieve this large vertical momentum transport. Our experiments with the Macquarie topography demonstrate that this can be achieved with a fairly realistic circulation in the channel. The interesting feature is that the eddies also find a way to structure the deep circulation in such a manner that the topographic form stress

can be effective in the balance and keep the influence of the unphysical bottom friction small.

Acknowledgments. We thank Uwe Mikolajewicz, Josef Oberhuber, and Ben Santer for valuable comments on the manuscript. We benefitted much from our cooperation with our colleagues Andreas Hense, Fred Kruse, and Jens Schröter. Special thanks are due to Marion Grunert for skillfully reproducing the diagrams.

APPENDIX

Evolution of the Boundary Layer Solution

Many of the figures in this paper show a boundary layer solution that is fairly broad and seems to be without a sound physical basis. The only interior friction scale is $(A_4/\epsilon)^{(1/4)}$ with which our parameters give a width of 17 km. Another intrinsic length scale is from the baroclinic eigenmode

$$(\nabla^2 - R_1^{-2})[\psi_1 - \psi_2] = 0, \qquad (A1)$$

which is 32 km in our application.

In order to study the evolution of the boundary layer (and to discriminate against possible errors of the code) we consider the flat bottom case where analytical expressions are easier to formulate. We assume zonal symmetry, reducing the problem to one spatial coordinate. The application of the Laplace transform on the time-dependent equations (3)

$$\Phi_i(p, y) = \int_0^\infty e^{-pt}\psi_i(t, y)dt \qquad (A2)$$

replaces the time derivative by a multiplication with p. The linear homogeneous system then reads

$$p\left(\frac{\partial^2}{\partial y^2} \Phi_1 - \frac{f_0^2}{g'H_1}(\Phi_1 - \Phi_2)\right) + A_4 \frac{\partial^6}{\partial y^6} \Phi_1 = 0 \quad (A3)$$

$$p\left(\frac{\partial^2}{\partial y^2} \Phi_2 + \frac{f_0^2}{g'H_2}(\Phi_1 - \Phi_2)\right)$$
$$+ \epsilon \frac{\partial^2}{\partial y^2} \Phi_2 + A_4 \frac{\partial^6}{\partial y^6} \Phi_2 = 0. \quad (A4)$$

For any p, the solution may be interpreted as the characteristic solution for the time-scale defined by p. For $p \neq 0$ we have an exponential behavior e^{ky} and (A4) yields

$$\Phi_2(y) = \frac{pf_0^2/(g'H_2)}{[pf_0^2/(g'H_2) - pk^2 - \epsilon k^2 - A_4k^6]} \Phi_1(y) \qquad (A5)$$

with $\lambda = k^2$ we get the characteristic equation

$$\begin{vmatrix} p[\lambda - f_0^2/(g'H_1)] + A_4\lambda^3 & pf_0^2/(g'H_1) \\ pf_0^2/(g'H_2) & \{p[\lambda - f_0^2/(g'H_2)] \\ & + \epsilon\lambda + A_4\lambda^3\} \end{vmatrix}$$
$$= 0 \quad (A6)$$

which yields a sixth-order polynomial $P(\lambda)$. Obviously, $\lambda = 0$ is one solution.

In the limiting case $p = 0$ for the stationary state, the system is decoupled; we have a third-order zero for λ (sixth-order for k) in the upper layer, allowing for fifth-order polynomials in y for Φ_1. In the lower layer the roots are at 0 and $(\epsilon/A_4)^{1/2}$ with the scale $(A_4/\epsilon)^{1/4}$.

For finite real p we have in addition to $\lambda = 0$ a second real root and four complex roots of P. The locations are easily found by a Newton iteration in the complex plain: starting with $\lambda = 0$ as the first root, the nth root is determined from the reduced polynomial:

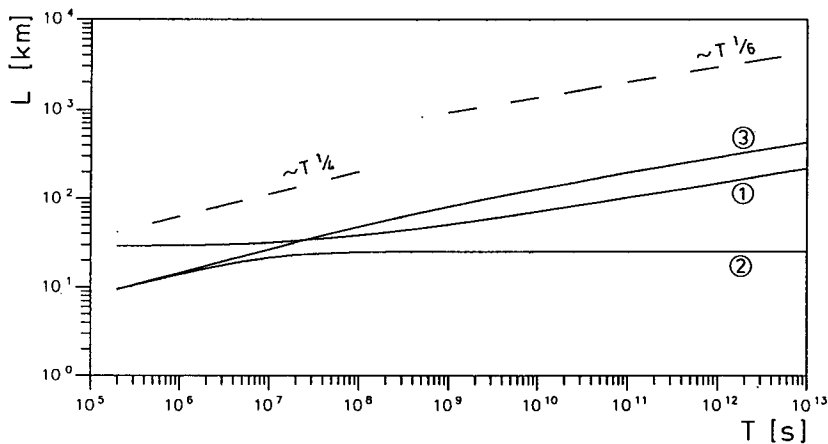$$F_n = F \cdot (\prod_{k=1}^{n=1} (\lambda - \lambda_k))^{-1}. \qquad (A7)$$

FIG. A1. Time development of different characteristic length scales of the boundary layer solution for case FB. Units are km for the length scales (y-axis) and seconds for the time scale (x-axis).

Figure A1 shows the real parts of the resulting k for real p, transformed into length scales as function of the time scale $1/p$. We can clearly identify three branches of length scales and three asymptotics L = const., $L \approx T^{1/4}$, and $L \approx T^{1/6}$, characteristic for the bottom friction and for the biharmonic friction acting on the relative vorticity and the vortex stretching, respectively. The first branch belonging to the real eigenvalue starts at the baroclinic Rossby radius and reaches for $T > 10^9$ s, the asymptotic $T^{1/6}$ behavior. The branches belonging to the complex eigenvalues start both for short time scales with $k = (\epsilon/A_4)^{1/4}$. At $T > 10^6$ s they split into two discrete branches, one of which approaches the bottom friction scale while the other approaches the asymptote $T^{1/6}$.

For the construction of the solution we have to perform the backtransformation

$$\psi = \int_{c-i\infty}^{c+i\infty} e^{pt}\Phi(p)dp \tag{A8}$$

where $\Phi = \Phi_0 + \sum_{i=1}^{12} \Phi_i$ and Φ_0 is obtained by insertion of the forcing $k_0\tau \sin k_0 y/p$ into (A3); in (A5) k^2 has to be replaced by $-k_0^2$ with $k_0 = \pi/Y$. The amplitude of ψ_0 is

$$\psi_0 = \tau k_0 \sin k_0 y \left\{ p \left[-\left(k_0^2 + \frac{f_0^2}{g'H_1} \right) p \right.\right.$$

$$\left.\left. + \frac{p^2(f_0^2/g'H_1)^2}{\epsilon k_0^2 + Ak_0^6 + p(k_0^2 + f_0^2/g'H_2)} - Ak_0^6 \right]\right\}^{-1}. \tag{A9}$$

The singularities are for our choice of parameters at p = 0, $p = -1.0569 \times 10^{-15}$ s^{-1}, and $p = -8.0088 \times 10^{-8}$ s^{-1}; the latter two obviously represent modifications of the imposed friction time scales. The backtransformation of ψ_0 can be found, after some reorganization of (A9), in tables (cf. Abramowitz and Stegun 1972). It is a sum of exponentials with the time-scales given by the singularities, similar to (16). For $t = 3.14 \times 10^8$ s (10 yr) we performed the integration at $c = 10^{-9}$ s^{-1} numerically by a simple trapezoidal rule. For each p, the amplitudes of Φ_i, $i = 1, \cdots, 12$ were determined by insertion of the boundary and auxiliary conditions. The effective e-folding width on this path has a maximum of 116 km at $p = c \pm i \cdot 2.5 \times 10^{-9}$. We found, indeed, the typical intensification of the zonal current towards the boundaries. The amplitudes of the zonal velocity relative to the value at the central latitude of the channel are 25% at the minima and 50% at the boundaries. The minima, for this t, are located 120 km off the boundaries.

All solutions discussed in this paper reflect this boundary layer structure, predominantly in the upper layer (see Figs. 3, 7, 16 and 17). For the length of integration (10^9 s) the e-folding width for real p is about 80 km. Figure A1 shows how this would increase with longer integration length.

REFERENCES

Abramowitz, M., and I. A. Stegun, 1972: *Handbook of Mathematical Functions.* Dover.

Arakawa, A., and V. R. Lamb, 1977: Computational design of the basic dynamical processes of the UCLA general circulation model. *Meth. Comput. Phys.,* **17,** 173–265.

Boyer, D. L., and J. R. Guala, 1972: Model of the Antarctic Circumpolar Current in the vicinity of the Macquarie Ridge. *Antarctic Oceanology II, Antarct. Res. Ser.,* **19,** D. E. Hayes, Ed. AGU, 79–93.

Bretherton, F. P., and D. B. Haidvogel, 1976: Two-dimensional turbulence above topography. *J. Fluid Mech.,* **78,** 129–154.

Bryan, K., and M. D. Cox, 1972: The circulation of the World Ocean: a numerical study. Part I, a homogeneous model. *J. Phys. Oceanogr.,* **2,** 319–335.

Bryden, H. L., 1983: The Southern Ocean. *Eddies in Marine Science,* A. R. Robinson, Ed., Springer, 265–277.

——, and R. A. Heath, 1985: Energetic eddies at the northern edge of the Antarctic Circumpolar Current in the South Pacific. *Progress in Oceanography,* Vol. 14, Pergamon, 65–87.

Chelton, D. B., M. G. Schlax, D. L. Witter and J. G. Richman, 1990: GEOSAT altimeter observations of the surface circulation of the Southern Ocean. *J. Geophys. Res.,* **95,** 7877–7903.

Cheney, R. E., J. G. Marsh and B. D. Beckley, 1983: Global mesoscale variability from collinear tracks of SEASAT altimeter data. *J. Geophys. Res.,* **88,** 4343–4354.

Colton, M. T., and R. R. P. Chase, 1983: Interaction of the Antarctic Circumpolar Current with bottom topography: an investigation using satellite altimetry. *J. Geophys. Res.,* **88,** 1825–1843.

Cox, M. D., 1975: A baroclinic numerical model of the world ocean: Preliminary results. *Numerical Models of Ocean Circulation,* Nat. Acad. Sci., 107–120.

Daniault, N., and Y. Ménard, 1985: Eddy kinetic energy distribution in the Southern Ocean from altimetry and FGGE drifting buoys. *J. Geophys. Res.,* **90,** 11 877–11 889.

de Szoeke, R. A., and M. D. Levine, 1981: The advective flux of heat by mean geostrophic motions in the Southern Ocean. *Deep-Sea Res.,* **28,** 1057–1085.

Gill, A. E., 1968: A linear model of the Antarctic Circumpolar Current. *J. Fluid Mech.,* **32,** 465–488.

——, and K. Bryan, 1971: Effects of geometry on the circulation of a three-dimensional Southern Hemisphere ocean model. *Deep-Sea Res.,* **18,** 685–721.

Gordon, A. L., 1972: On the interaction of the Antarctic Circumpolar Current and the Macquarie Ridge. *Antarctic Oceanology II, Antarct. Res. Ser.,* **19,** D. E. Hayes, Ed., AGU, 71–78.

——, E. Molinelli and T. Baker, 1978: Large-scale relative dynamic topography of the Southern Ocean. *J. Geophys. Res.,* **83,** 3023–3032.

Han, Y.-J., 1984: A numerical world ocean general circulation model. Part I. Basic design and barotropic experiment. *Dyn. Atmos. Oceans,* **8,** 107–140.

Hidaka, K., and M. Tsuchiya, 1953: On the Antarctic Circumpolar Current. *J. Mar. Res.,* **12,** 214–222.

Holloway, G., 1987: Systematic forcing of large-scale geophysical flows by eddy-topography interaction. *J. Fluid Mech.,* **184,** 463–476.

Houry, S., E. Dombrowsky, P. De Mey and J.-F. Minster, 1987: Brunt–Väisälä frequency and Rossby radii in the South Atlantic. *J. Phys. Oceanogr.,* **17,** 1619–1626.

Ivchenko, V. O., 1985: On the parameterization of the eddy flows of geostrophic potential vorticity in zonal ocean currents. *Izv., Atmos. Oceanic Physics,* **21**(8), 660–664.

Johnson, G. C., and H. L. Bryden, 1989: On the size of the Antarctic Circumpolar Current. *Deep-Sea Res.,* **36,** 39–53.

Kamenkovich, V. M., M. N. Koshlyakov and A. S. Monin, 1986: *Synoptic Eddies in the Ocean.,* D. Reidel, 433 pp.

Koblinsky, C., 1988: GEOSAT vs. SEASAT. *Eos,* **69**(44), 1026.

Lutjeharms, J. R. E., 1982: Baroclinic volume transport in the Southern Ocean. *J. Phys. Oceanogr.,* **12,** 3–7.

Marshall, J. C., 1981: On the parameterization of geostrophic eddies in the ocean. *J. Phys. Oceanogr.,* **11,** 257–271.

McCartney, M. S., 1976: The interaction of zonal currents with topography with applications to the Southern Ocean. *Deep-Sea Res.,* **23,** 413–427.

McWilliams, J. C., 1977: A note on a consistent quasi-geostrophic model in a multiply connected domain. *Dyn. Atmos. Oceans,* **1,** 427–441.

——, and J. H. S. Chow, 1981: Equilibrium geostrophic turbulence. I: A reference solution in a β-plane channel. *J. Phys. Oceanogr.,* **11,** 921–949.

——, W. R. Holland and J. H. S. Chow, 1978: A description of numerical Antarctic Circumpolar Currents. *Dyn. Atmos. Oceans,* **2,** 213–291.

Munk, W. H., and E. Palmén, 1951: Note on the dynamics of the Antarctic Circumpolar Current. *Tellus,* **3,** 53–55.

Olbers, D. J., and M. Wenzel, 1989: Determining diffusivities from hydrographic data by inverse methods with applications to the circumpolar current. *Modelling the Ocean General Circulation and Geochemical Tracer Transport.* J. Willebrand and D. L. T. Anderson, Eds., NATO ASI Series C, Kluwer Academic, 95–122.

Patterson, S. L., 1985: Surface circulation and kinetic energy distributions in the Southern Hemisphere oceans from FGGE drifting buoys. *J. Phys. Oceanogr.,* **15,** 865–884.

Reid, J. L., 1986: On the total geostrophic circulation of the South Pacific Ocean: flow patterns, tracers, and transports. *Progress in Oceanography,* Vol. 16, Pergamon, 1–61.

Richtmyer, R. D., 1967: *Difference Methods for Initial-Value-Problems.* Interscience, 2nd ed.

Spillane, M., 1978: Topographic generation of intermediate-scale motions by wind-driven currents—a model for the circulation in the vicinity of the Indian-Antarctic Ridge. *Dyn. Atmos. Oceans,* **2,** 427–453.

Treguier, A. M., and J. C. McWilliams, 1990: Topographic influences on wind-driven, stratified flow in a β-plane channel: an idealized model for the Antarctic Circumpolar Current. *J. Phys. Oceanogr.,* **20,** 321–343.

Wolff, J.-O., and D. J. Olbers, 1989: The dynamical balance of the Antarctic Circumpolar Current studied with an eddy resolving quasi-geostrophic model. *Mesoscale–Synoptic Coherent Structures in Geophysical Turbulence,* J. C. J. Nihoul and B. M. Jamart, Eds., Elsevier, 435–458.